https://doi.org/10.1016/j.electacta.2020.135809

Metal–Organic Framework-Derived $MnO/CoMn_2O_4$@N–C Nanorods with Nanoparticle Interstitial Decoration in Core@Shell Structure as Improved Bifunctional Electrocatalytic Cathodes for Li–O_2 Batteries

Amrita Chatterjee [a,b] *and Siu Wing Or* [a,b]*

[a] Department of Electrical Engineering, The Hong Kong Polytechnic University, Hung Hom, Kowloon, Hong Kong.

[b] Hong Kong Branch of National Rail Transit Electrification and Automation Engineering Technology Research Center, Hong Kong.

* Corresponding author: Professor Siu Wing Or. Email: eeswor@polyu.edu.hk. ORCID ID: 0000-0003-2536-5658

Abstract

Core@shell-structured, hierarchically porous manganese oxide/cobalt manganite@nitrogen-doped carbon ($MnO/CoMn_2O_4$@N–C) nanorods with interstitially decorated $CoMn_2O_4$ nanoparticles are synthesized via one-step carbonization of metal–organic framework (MOF)-coated α-manganese oxide (α-MnO_2@ZIF-67) nanorods and are evaluated as bifunctional electrocatalytic cathodes for Li–O_2 batteries (LOBs) to improve the bifunctionality, specific discharge capacity, and cyclability of α-MnO_2 nanorod cathode-based LOBs. The $MnO/CoMn_2O_4$@N–C nanorods feature a MnO nanorod core with $CoMn_2O_4$ nanoparticle interstitial decoration, both coated by an N–C conductive shell. The MnO core renders Mn active sites and oxygen vacancies, while the $CoMn_2O_4$ interstitial decoration gives additional Mn, Co active sites, thereby enhancing bifunctional electrocatalytic ORR–OER. The N–C shell increases

electronic conductivity, hierarchical porosity, specific surface area, and protects the core and interstitial decoration against lithium peroxide (Li_2O_2) passivation. The improved structural features allow the MnO/$CoMn_2O_4$@N–C nanorod cathode-based LOB cells to exhibit superior full specific discharge capacity of 8625 mAh·g^{-1} and cyclability of 48 discharge–charge cycles at 200 mA·g^{-1} specific current and 2000 mAh.g^{-1} limited specific discharge capacity compared to their α-MnO_2 nanorod counterparts. An ORR–OER mechanism is proposed to describe the interesting formation of particle- and film-type Li_2O_2 deposits at different cycles for the MnO/$CoMn_2O_4$@N–C nanorod cathodes. Such MOF-derived, interstitial nanoparticle-decorated nanoarchitectures can lead to high-performance tunable bifunctional electrocatalysts.

Highlights

- MOF-derived core@shell MXNC nanorods with interstitial decoration was developed
- Mn, Co, and oxygen vacancies from core and interstitial impart bifunctionality
- Conductive high surface area N–C shell protect the core against passivation
- MXNC nanorods show higher cycles and capacity as LOB cathodes than α-MnO_2 nanorods
- Tunable method for high surface area interstitially decorated bifunctional cathode

Keywords *Bifunctional, electrocatalytic cathodes, core@shell structure, metal–organic framework, nanoparticle interstitial decoration, lithium-oxygen batteries*

1. Introduction

Lithium–oxygen batteries (LOBs) have gained a tremendous popularity in recent years due to their ultrahigh theoretical specific capacity in comparison with traditional Li-ion batteries (LIBs). In particular, the specific energy density of non-aqueous LOBs at discharge state (~3460 $Wh \cdot kg^{-1}$) is approximately 10 times higher than the LIBs, while its value at charge state (~11,680 $Wh \cdot kg^{-1}$) is nearly equivalent to the gasoline [1]. These have made envisioning the application prospects of LOBs as clean energy sources in pure electric vehicles. However, the main challenges for the practical applications of LOBs are their limited specific discharge capacity, poor rate capability, high over-potential, and low cyclability. These hindrances mainly result from the sluggish kinetics of oxygen reduction reaction (ORR) and oxygen evolution reaction (OER). Moreover, the deposition of insoluble and insulating discharge products in form of lithium peroxide (Li_2O_2) and their intermediates occlude the electrocatalytic sites of cathodes and reduce the cyclability of the LOBs [2,3]. Thus, it is necessary to design and develop energetically stable bifunctional electrocatalytic cathodes with improved active sites, oxygen vacancies, and electronic conductivity to exploit the advantages of LOBs.

Transition metal oxides, as tailorable and user-friendly materials, are promising candidates for LOB cathodes. Owing to the faster electron transport and higher electronic conductivity [4], the 1-D structure of α-MnO_2 nanorods/nanowires is more favorable for bifunctional electrocatalysts than the others such as hollow spheres, nanoparticles or nanotubes [5,6]. However, at higher cycles, α-MnO_2 nanorods suffer from deposition of insulating discharge products and low cyclability [7]. Though core@shell-structured CNT@MnO and MnO_2 nanotube@nitrogen-doped exfoliated graphene can impart conductivity and reduce passivation of electrocatalytic core to some extent [8,9], their bifunctional activities and specific surface areas are both far from being

the state-of-the-art. On the other hand, while bimetallic oxides such as $CoMn_2O_4$ and $MnCo_2O_4$ nanoparticles have improved bifunctional activities in aprotic LOBs [10–12], they are subject to rapid passivation and low conductivity. It would be ideal to combine the α-MnO_2 nanorods cores with N–C (nitrogen-doped carbon) shells and decorate them with bimetallic oxide nanoparticles to obtain the necessary conductivity, protection against passivation, and bifunctionality in electrocatalytic cathodes for the LOB cells. However, synthesis of α-MnO_2 and N–C shell is a tedious process by itself. Further introducing bimetallic oxide nanoparticles in such a core@shell structure require additional steps of doping. To this end, our objective in this article is to simplify the cumbersome synthesizing process of α-MnO_2@N–C shell nanorods with bimetallic $CoMn_2O_4$ nanoparticle decorations and achieve improved bifunctionality of α-MnO_2 nanorods. We propose and demonstrate a one-step carbonization process to develop an integrated nanoarchitecture of MnO/$CoMn_2O_4$@N–C nanorods consisting of a core@shell structure of MnO core with interstitially located cobalt manganite nanoparticle ($CoMn_2O_4$), both encapsulated by a N–C shell. The introduction of the synergistic, bimetallic oxide nanoparticles at the interstitial sites alter the lattice structure and charge transfer [13] between the surrounding cores and shells, thereby providing an additional boost to the bifunctional electrocatalytic properties of the nanoarchitectures. This, in turn is reflected in the enhanced performance of the LOBs with MnO/$CoMn_2O_4$@N–C nanorod cathodes compared to α-MnO_2 nanorod cathodes.

The applications of metal–organic frameworks (MOFs) prove beneficial in synthesizing the aforementioned cathode. The nitrogen ligands act as the source of N–C shell, while their metal nodes combine with the metallic core to develop interstitial bimetallic oxide decorations. We exploit these properties and perform one-step carbonization of the MOFs to synthesize cathodes for the LOBs. In addition, the carbonization of the MOFs also improves the specific surface area

of the MnO/$CoMn_2O_4$@N–C nanorods. MOF-derived high surface area hollow shells such as Co-Mn-O nanocubes, ZnO/$ZnFe_2O_4$/C nanocages, and Co,N-doped carbon polyhedra have gained huge impact as energy storage materials in batteries and supercapacitors [14–17]. However, MOF-derived core@shell-structured 1-D nanomaterials with interstitially decorated nanoparticles have scarcely been explored as LOB cathodes.

In this work, we have developed hierarchically porous 1-D core@shell-structured MnO/$CoMn_2O_4$@N–C nanorods with interstitially decorated nanoparticles, where MnO, $CoMn_2O_4$, and N–C can be obtained simultaneously via one-step carbonization process. From here onwards, we designate MnO/$CoMn_2O_4$@N–C nanorods as MXNC nanorods, where M represents MnO (manganese oxide), X represents $CoMn_2O_4$ (cobalt manganite), and N–C represents nitrogen-doped carbon. It is to be noted that, in this study, ZIF-67 (Zeolitic Imidazole Framework-67) has been chosen as a suitable MOF for sheathing the α-MnO_2 nanorods. The interstitial $CoMn_2O_4$ decorated nanoparticles are derived from the Co nodes of ZIF-67, while the N–C shell is derived from the nitrogen containing ligands. The schematic of the synthesis process has been shown in ***Scheme 1***. The carbonization of the core@shell α-MnO_2@ZIF-67 nanorods at high temperature under argon results in: (i) reduction of α-MnO_2 to multivalent MnO cores that act as oxygen vacancy-induced bifunctional electrocatalytic sites; (ii) decoration of interstitial $CoMn_2O_4$ nanoparticles that enhances the bifunctionality through Mn, Co bimetallic synergism; (iii) encapsulation of the cores with electrically conductive N–C shell derived from the ZIF-67, that improves the electron migration as well as protects the core against Li_2O_2 deposition; and (iv) increases the specific surface area and hierarchical porosity for easy diffusion of Li^+ ions and oxygen molecules.

These unique features have enabled the MXNC nanorods to act as better bifunctional cathodes compared to bare α-MnO_2 nanorods or carbonized ZIF-67 individually. The applications of such MOF-derived nanoarchitectures is relatively new in the field of LOBs. To gain new insights on the advantages of such materials, we have conducted a detailed comparison of LOB performances with parental core, individual shell, and core@shell nanorods carbonized at different temperatures. The electrochemical characterizations of fresh and dead cathodes, and formation of various morphologies of Li_2O_2 at different cycles supported the proposed mechanism of ORR–OER on the electrocatalytic surface of MXNC nanorod cathodes. Finally, this work emphasizes the facile one-step carbonization process to achieve MOF-derived shells with interstitially decorated nanoparticles and their roles as vital supplement to bolster the cyclability and bifunctionality of α-MnO_2 nanorods as air-cathodes. Interestingly, such nanoparticle decorations may be tuned by wise choice of MOFs for wide range of catalytic and device applications.

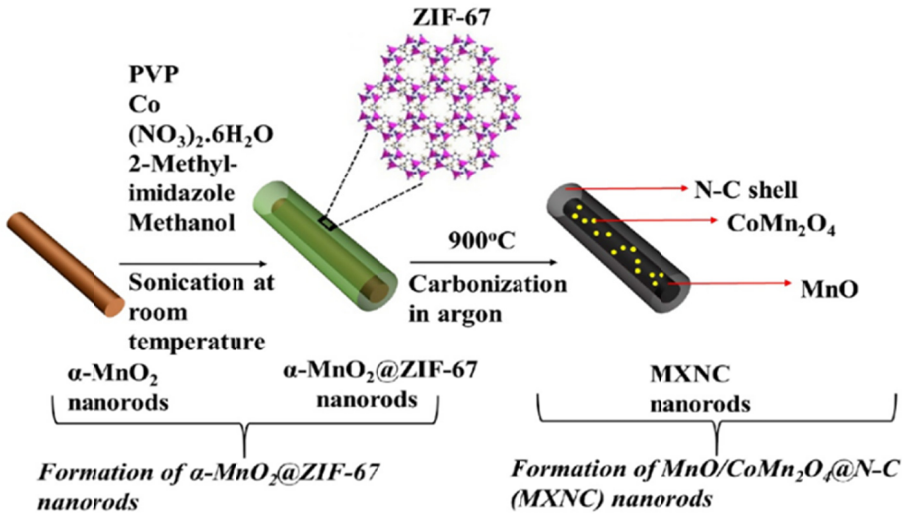

Scheme 1. Schematic representation of the synthesis of MXNC nanorods.

2. Experimental Section

2.1 Materials

The following materials were used: potassium permanganate ($KMnO_4$), ammonium fluoride (NH_4F), cobalt nitrate hexahydrate ($Co(NO_3)_2.6H_2O$), 2-methylimidazole (HMeIM), polyvinylpyrole (PVP) with M.W-50,000, methanol, absolute ethanol, de-ionized water, polytetrafluoroethylene (PTFE), isopropanol, Super P carbon, 16 mm diameter discs of GDS230 carbon paper, Whatmann glass fiber GF/D, and lithium foil, lithium bis(trifluoromethanesulfonyl)imide (LiTFSI), tetraethylene glycol dimethyl ether (TEGDME). The non-aqueous electrolyte solution was composed of 1(M) LiTFSI in TEGDME. All chemicals were obtained from Acros Organic with 98–99% purity and used without further treatment, unless otherwise specified.

2.2 Synthesis of nanorods

***Synthesis of α-MnO_2 nanorods*:** The α-MnO_2 nanorods were synthesized according to previous literature [4]. Briefly, an aqueous solution of 0.1 g potassium permanganate, 0.9 g ammonium fluoride, and 40 mL of water was prepared under magnetic stirring. The solution was heated at 200^{o}C for 24 h in an air oven. The resulting solution was cooled to room temperature and the brown precipitate obtained was filtered and washed with distilled water for several times. The precipitate was dried at 80^{o}C for 12 h.

***Synthesis of MnO/$CoMn_2O_4$@N–C (MXNC) nanorods*:** In order to prepare the core@shell MXNC nanorods, 50 mg of α-MnO_2 nanorods were dispersed in 10 mL methanol and ultrasonicated for 15 min. A solution made of 250 mg PVP dissolved in 5 mL of methanol was

added to the α-MnO_2 nanorods dispersion. The mixed solution was ultrasonicated for 10 min to ensure uniform functionalization of the α-MnO_2 nanorods with the PVP surfactant. To this was added a solution containing 328 mg (4 mmol) HMeIM dissolved in 5 mL methanol and the combined solution was ultrasonicated for 10 min. Finally, a solution of 291 mg (1 mmol) $Co(NO_3)_2.6H_2O$ dissolved in 5 mL methanol was added dropwise into the mixture containing α-MnO_2 nanorods, PVP, and HMeIM. The mixture was ultrasonicated for 10 min and kept at rest for 24 h at room temperature. The precipitate obtained (α-MnO_2@ZIF-67 nanorods) was washed repeatedly with methanol and dried in vacuum at 80°C/12 h. The precipitate was calcined in argon atmosphere till 900°C at 2°C·min^{-1} and maintained at that temperature for 3 h. The schematic of the synthesis process has been shown in ***Scheme 1***. For the purpose of comparison, the previously synthesized precipitate of α-MnO_2@ZIF-67 nanorods was carbonized in argon atmosphere till 650°C at 2 °C·min^{-1} and maintained at that temperature for 3 h. The sample was named as *MXNC nanorods-650*.

As a control, pure ZIF-67 was also prepared. Typically, a solution was prepared by dissolving 291 mg $Co(NO_3)_2.6H_2O$ in 15 mL methanol. Another solution was prepared by dissolving 328 mg HMeIM in 5 mL methanol. The two solutions were mixed and ultrasonicated for 10 min and kept at rest at room temperature for 24 h [18]. In order to compare the full specific discharge capacity of the shell only, the synthesized ZIF-67 was calcined in argon atmosphere till 900°C at 2 °C·min^{-1} and maintained at that temperature for 3 h. It was named as *ZIF-67-900*.

2.3 Physicochemical characterizations of nanorods

The crystallographic information of the samples was obtained from the XRD (X-ray diffraction) patterns recorded using a diffractometer (Rigaku Smartlab X-Ray, operated at 40 kV

using a Cu Kα radiation). The Rietveld analyses of the XRD patterns were performed with MAUD. The elemental analysis and oxidation states of the samples were obtained from XPS (X-ray photoelectron spectroscopy) performed with Kratos Axis Ultra DLD and referenced to the C1*s* neutral carbon peak at 285 eV. The thermal stability and carbon content were determined by heating the samples under nitrogen and oxygen respectively at $10^{o}C \cdot min^{-1}$ in thermo-gravimetric analyzer (Mettler Toledo TGA/DSC3+). The surface area and pore volumes of the samples were analyzed by N_2 physisorption at 77 K in a surface analyzer (Micrometrics ASAP 2020). To identify the nature of the carbon, the Raman spectra of the samples were collected with Renishaw Raman spectrometer. The morphologies of the samples were determined from the STEM (Scanning Transmission Electron Microscope) and SEM (Scanning Electron Microscope) using JEOL JEM-2100F microscope and TESCAN VEGA microscope respectively. The electrical conductivities of the cathodes were measured using a four-probe resistivity/Hall system (HK5500PC, Bio-Rad). For post-mortem characterizations, the discharged cathodes were washed with TEGDME before conducting any of the above characterizations.

2.4 Fabrication of cathodes and their LOB cells

For the preparation of the cathodes, a homogeneous ink was composed of 60% MXNC nanorods, 20% Super P carbon, and 20% PTFE dissolved in isopropanol. The dispersion was drop-casted on carbon paper discs (1.6 cm diameter, 0.019 cm thick, 2 cm^2 area) and dried in vacuum at $120^{o}C$. The total mass loading of the MXNC nanorods and Super P was 1±0.05 $mg \cdot cm^{-2}$. A cathode made of 80% Super P and 20% PTFE with same mass loading was composed to compare the performance efficiency of the MXNC nanorods cathodes toward the LOBs.

The LOB cells were fabricated using an EQ-STC-Li-air split test cell ***(Figure S1)*** from MTI inside a glove box filled with argon gas (O_2 and moisture content < 0.1 ppm). The aforementioned cathode prepared with MXNC nanorods, Whatmann glass fiber separator, lithium anode, and 60 µL of electrolyte were assembled into the EQ-STC-Li-air cell and sealed tightly with screws. The cells were flushed with 99.7% pure oxygen supply for 0.5 h and kept for 3 h in open circuit condition before performing the electrochemical measurements.

2.5 Electrochemical characterizations of LOB cells

The galvanostatic discharge–charge profiles (vs. Li^+/Li) of the 2-electrode system LOB cells were obtained from a LANDT 2001 CT battery tester within the voltage window of 2–4.5 V and at different specific current densities. The cyclic ability was evaluated at a specific current density of 200 $mA \cdot g^{-1}$ and a limited specific capacity of 2000 $mAh \cdot g^{-1}$. The rate performances were executed at a limited specific capacity of 2000 $mAh \cdot g^{-1}$ and increasing specific current densities of 100, 200, and 400 $mAh \cdot g^{-1}$ and back to 100 $mAh \cdot g^{-1}$. The specific discharge capacity and specific current densities were calculated based on the active material mass loading of the cathode. The Cyclic Voltammetry (CV) was conducted with a CHI 660E Electrochemical Impedance Spectroscope (EIS) at a voltage sweep rate of 5 $mV \cdot s^{-1}$ and voltage range of 2–4.5 V. The impedance spectrum for Nyquist plots of the LOB cells at different stages were recorded at a perturbation amplitude of 5 mV and frequency range of 10^{-3} to 10^5 Hz. The EIS impedance spectra was fitted to equivalent circuit by ZView software.

3. Results and discussion

3.1 Physicochemical properties of MXNC nanorods

The physicochemical characterizations of MXNC nanorods are compared with α-MnO_2 nanorods, ZIF-67, and α-MnO_2@ZIF-67 nanorods. For that the purpose, XRD, N_2 physisorption, Raman spectroscopy, TGA, XPS, SEM, TEM, and 4-probe conductivity measurement have been used. An ideal air-cathode should have high surface area and conductivity. To develop the conductive MOF-derived N–C shell, it is necessary to optimize the carbonization temperature of the core@shell α-MnO_2@ZIF-67 nanorods. The TGA analysis of α-MnO_2@ZIF-67 nanorods performed under N_2, in ***Figure S2 (a)*** shows that at 310^{o}C, the solvent molecules trapped in the pores of ZIF-67 were removed. Further heating till ~500^{o}C was accompanied with slight loss indicating the complete activation of the ZIF-67. The sharp weight loss from 500 to 900^{o}C was due to the decomposition of the ligands and collapse of the ZIF-67 framework structure. Since the graphitization was completed at 900^{o}C, therefore, it was selected as the optimum temperature for carbonization.

Crystal structure analysis: The XRD pattern and crystal structure of the core precursor, α-MnO_2 nanorods in ***Figures S3(a-b)***, confirm their phase purity and body-centered tetragonal phase (JCPDS card no. 44-0141, space group I4/m) [19]. The MnO_6-octahedral units of α-MnO_2 arrange in form of chain along the 2×2 tunnels [20]. The Rietveld refinement of the XRD pattern of shell precursor, pristine ZIF-67 crystals ***(Figure S3(c-d))***, are in agreement with the sodalite cage type structure (space group I4/3m) [21]. The XRD pattern of the core@shell MXNC nanorods in ***Figure 1(a)*** shows the characteristic peak of graphitic carbon (002) at 2θ=23.8^o. The carbonization of the thermo-labile ligands of the ZIF-67 and the promotional activity of cobalt ions are responsible for the graphitization of carbon [22]. The planes of (111), (200), and (311) belong to the cubic phase MnO (JCPDS-07-0230, space group Fm-3m). The remaining peaks have been assigned to the crystal planes of (101), (112), (211), (220), and (413) of tetragonal

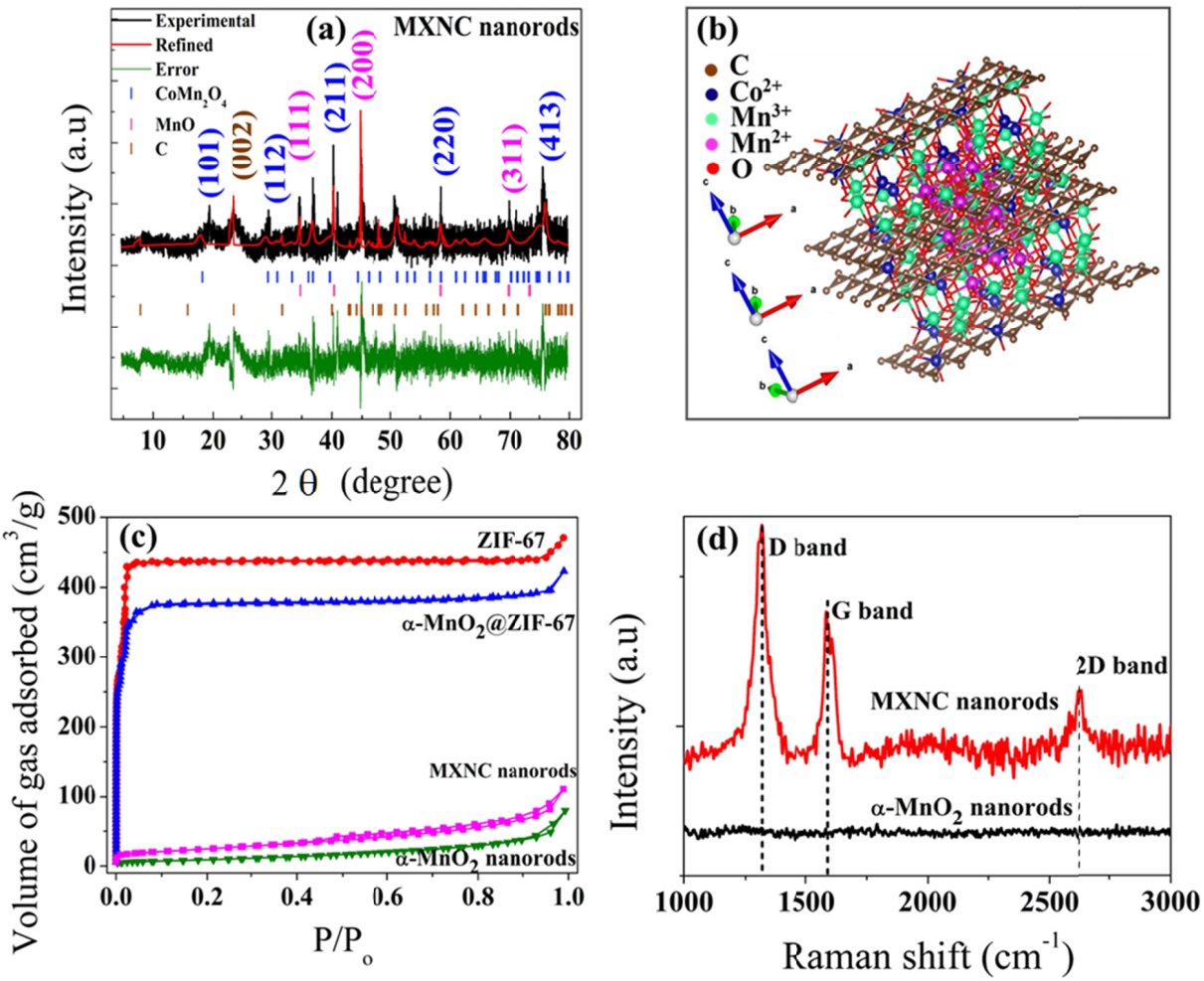

Figure 1. (a) XRD pattern and Rietveld refinement of MXNC nanorods, (b) crystal structure of MXNC nanorods, (c) N_2 adsorption-desorption isotherms of ZIF-67, α-MnO_2@ZIF-67 nanorods, MXNC nanorods and α-MnO_2 nanorods and (d) Raman shift spectra of α-MnO_2 and MXNC nanorods.

---

phase $CoMn_2O_4$ (JCPDS-77-0471, space group I41/amd), which was formed during carbonization. The cobalt oxide generated during the decomposition of ZIF-67 reacted with the MnO at 900°C to form interstitial $CoMn_2O_4$ nanoparticles [23]. The probable structure of MXNC

nanorods obtained from Rietveld refinement of the XRD pattern ***(Figure 1(b))*** corresponds with the core@shell-structure, where the core MnO with interstitial $CoMn_2O_4$ nanoparticles are encapsulated with a N–C shell. The Rietveld refinement parameters of the α-MnO_2 nanorods, ZIF-67, and MXNC nanorods have been listed in ***Table S1***.

Surface area and pore size distribution analysis: Despite the high temperature carbonization of α-MnO_2@ZIF-67 nanorods, the resulting MXNC nanorods showed twice the specific surface area than the α-MnO_2 nanorods. The Type I isotherm of ZIF-67 indicates their microporous nature [24], while the Type II isotherm of α-MnO_2 nanorods indicates their mesoporosity [4]. It is seen from ***Figure 1(c)*** that individually, α-MnO_2 nanorods and ZIF-67 possess specific surface area of 38.60 and 1498.31 $m^2 \cdot g^{-1}$, respectively. The successful inclusion of the α-MnO_2 nanorods as cores inside the ZIF-67 framework reduced the specific surface area of α-MnO_2@ZIF-67 nanorods to 806.44 $m^2 \cdot g^{-1}$. After carbonization, the MXNC nanorods formed, have a high specific surface area of 80.87 $m^2 \cdot g^{-1}$ owing to the shell derived from the outer ZIF-67. The Type IV isotherm and H4 hysteresis loop reflects the mesoporosity of the MXNC nanorods. The destruction of the framework of ZIF-67 and generation of nanoscale voids due to migration of Co atoms during carbonization resulted in the mesoporosity of the shell [15,25]. Pore size distribution analysis in ***Figure S4*** shows that the α-MnO_2 nanorods have mesopores at pore widths of ~ 4.6 nm (contributed from the 2×2 tunnels [4,26]) and 37.0 nm. Whereas, the hierarchically porous MXNC nanorods have micropores and mesopores at various pore widths from 1–68.5 nm. The small pore size of the 2×2 tunnels in α-MnO_2 nanorods is considered to be unfavorable for the fast diffusion of Li^+ ions and oxygen molecules [8,23,27]. In contrast the wide range of large sized mesopores in MXNC nanorods provide short diffusion pathways for the penetration and transportation of the Li^+ ions and oxygen molecules. The high surface area

and hierarchical pore size distribution in MXNC nanorod cathodes enhance the mass transfer and reaction rate of ORR–OER in the LOBs [28].

Chemical state and composition analysis: The Raman spectroscopy of MXNC nanorods in ***Figure 1(d)*** shows two peaks at 1363 and 1587 cm^{-1} corresponding to the D and G-bands respectively. The D-band arises from the sp^3 disordered carbon while the G-band indicates the co-existence of sp^2 graphitic carbon [29]. The 2D-band at 2220 cm^{-1} is attributed to the highly graphitic layers of carbon formed due to the catalytic effect of Co on the graphitization process at high carbonization temperature [30]. During carbonization, the imidazole linkers of ZIF-67 surrounding the cobalt ions get catalytically converted to graphitic carbon. In spite of the formation of the highly developed graphitic layers of carbon as indicated by the peak at 2220 cm^{-1}, the ratio of I_D/I_G is ~1.48. This anomaly is due to the presence of fair amount of edge defects imparted by the cobalt and nitrogen on the carbon shell derived from ZIF-67 [23]. Such defects are also induced during the high temperature carbonization process when α-MnO_2 is reduced to MnO [31]. In contrast no such D and G-bands are observed in case of α-MnO_2 nanorods due to the absence of a MOF-derived N–C shell. The carbon content of MXNC nanorods was determined by their calcination in air. It was calculated from ***Figure S2(b)*** that MXNC nanorods contain ~13 wt. % carbon in its structure. It is surmised that the carbon content is combination of disordered and graphitic in nature. The graphitic carbon content corresponds to the (002) peak in the XRD patterns.

The successful formation of core@shell-structured MXNC nanorods with interstitial $CoMn_2O_4$ decoration is further confirmed from the overall XPS spectra ***(Figure S5)*** and the

Table 1. Atomic concentration of elements by XPS

	Mn	Co	O	N	C
α-MnO_2 nanorods	35.68	-	64.32	-	-
α-MnO_2@ZIF-67 nanorods	3.11	5.64	11.12	16.67	63.46
MXNC nanorods	2.72	1.18	7.12	0.76	88.22
MXNC nanorod-650	2.86	1.35	9.11	1.02	85.66

corresponding atomic concentration analysis ***(Table 1)***. After the carbonization process of α-MnO_2@ZIF-67 nanorods, the nitrogen and cobalt content reduced, and carbon content increased. The Mn 2*p* spectrum of α-MnO_2 nanorods in ***Figure 2(a)*** has two peaks corresponding to Mn $2p_{3/2}$ (641.6 eV) and Mn $2p_{1/2}$ (653.2 eV). The deconvolution of the peaks [20,32] and spin energy difference of 11.7 eV between Mn $2p_{3/2}$ and Mn $2p_{1/2}$ orbitals confirm the presence of Mn^{4+} ions in α-MnO_2 nanorods [33]. Due to the formation of oxygen vacancies during reduction of MnO_2 to MnO at carbonization temperature, a blue shift of Mn 2*p* peaks is observed for MXNC nanorods ***(Figure 2(b))*** [34]. The deconvolution of Mn 2*p* peaks of MXNC nanorods in ***Figure 2(c)*** indicate the presence of Mn^{2+} and Mn^{3+} as the dominant phases after the carbonization process. It is in agreement with the XRD crystal structure ***(Figure 1(b))***, where Mn^{2+} and Mn^{3+} occupy the tetrahedral and octahedral sites respectively. It had been confirmed previously from the XRD pattern that Co atoms in MXNC nanorods exist as $CoMn_2O_4$ phase. The Co 2*p* spectrum of MXNC nanorods in ***Figure 2(d)*** show the presence of multivalent Co^{2+} and Co^{3+}, which arise due to polaron hopping during carbonization. The activation energy

between the Co^{2+} and Co^{3+} is comparable. This induces the increase in oxidation state of Co^{2+} via electronic transfer through polaron hopping between the Mn^{3+} and Co^{2+}. Consequently, the Co^{3+} concentration increases, and they migrate from the tetrahedral sites to the octahedral sites. The vacancy left in the tetrahedral sites are thus filled by the Mn^{3+} ions which get reduced to Mn^{2+} ions in the process [34,35]. The presence of such multivalent Co and Mn ions in the interstitials provide the additional boost to bifunctional activity of the MXNC nanorods.

It is seen from ***Figure 2(e)***, that the deconvolution of N 1*s* spectrum of MXNC nanorods, confirms the presence of pyridinic (398.8 eV) and graphitic (400.1 eV)nitrogen [36]. The nitrogen content of the carbon matrix is imparted by the imidazole linkers of the ZIF-67. The pyridinic nitrogen atoms bonded to the carbon matrix are strong electron acceptors. They donate one electron to the conjugated π bond system and possess one lone pair of electrons. Consequently, a net positive charge is imparted on the neighboring carbon atoms. This favors the adsorption of oxygen atoms and attracts the electrons from anode towards them to facilitate the ORR [37].

The C 1*s* spectrum of MXNC nanorods in ***Figure 2(f)*** indicates the existence of C-C/C=C (284.6 eV), C-N (285.2 eV), C-O (286.7 eV) and C=O (289 eV) [38]. Therefore, it could be concluded that the carbon shell was graphitic in nature with nitrogen doping.

The O 1*s* spectrum of MXNC nanorods in ***Figure 3(a)*** shows a red shift compared to α-MnO_2 nanorods. This is due to the presence of oxygen vacancies [39] and interactions of the O atoms with Co, N, and C species. The deconvoluted O1*s* spectrum of MXNC nanorods in ***Figure 3(c)*** confirms the presence of lattice oxygen (529.8 eV), loosely bound oxygen from water molecules on the surface of MXNC nanorods (531.2 eV) [40], and adsorbed oxygen (532.9 eV). The adsorbed oxygen content is a significant parameter to verify the presence of oxygen vacancies. It

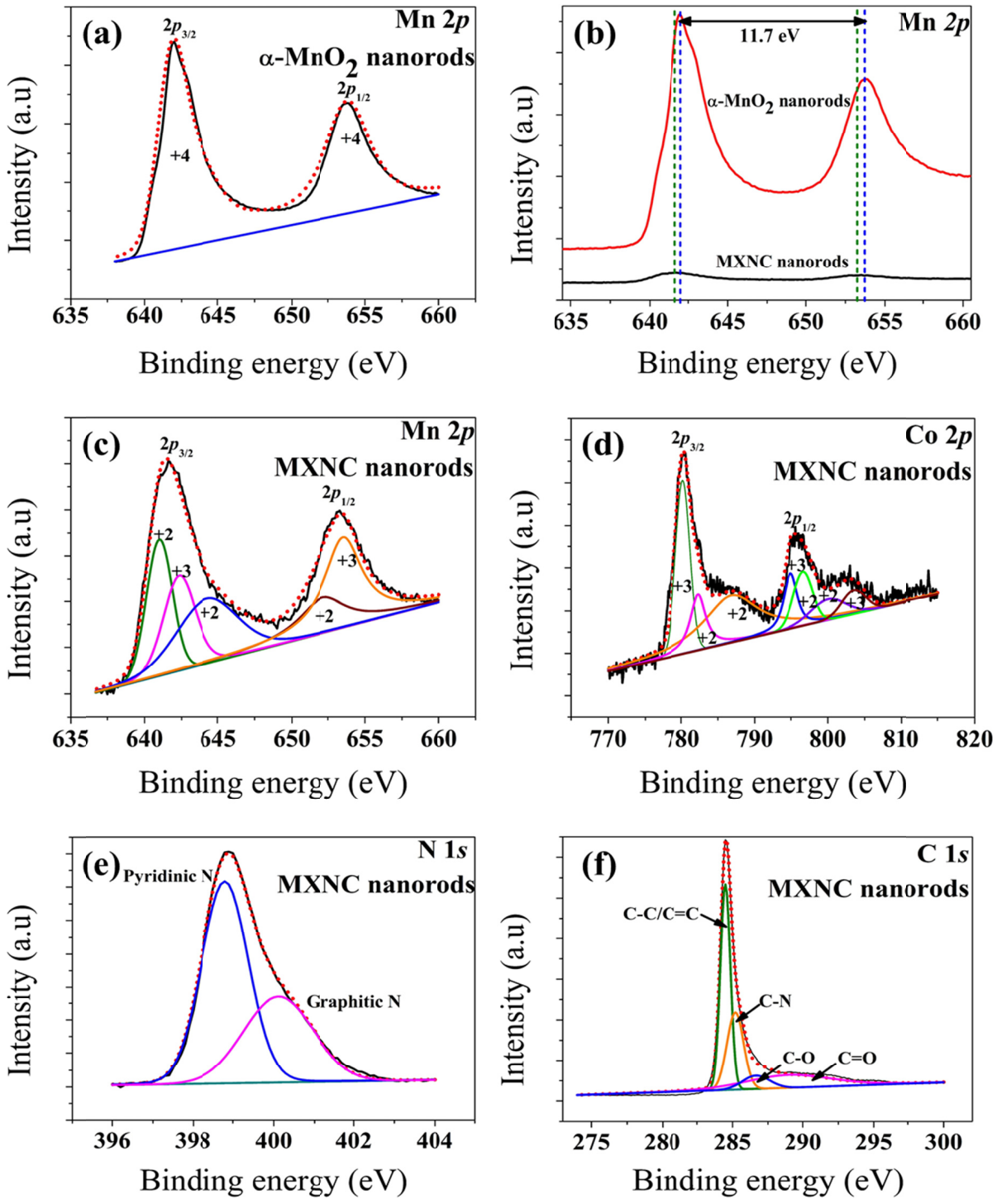

Figure 2. XPS spectra: (a) Mn 2*p* of α-MnO_2 nanorods, (b) shift comparison of Mn 2*p* spectra of α-MnO_2 and MXNC nanorods, (c) Mn 2*p* of MXNC nanorods, (d) Co 2*p* of MXNC nanorods, (e) N 1*s* of MXNC nanorods, and (f) C 1*s* of MXNC nanorods.

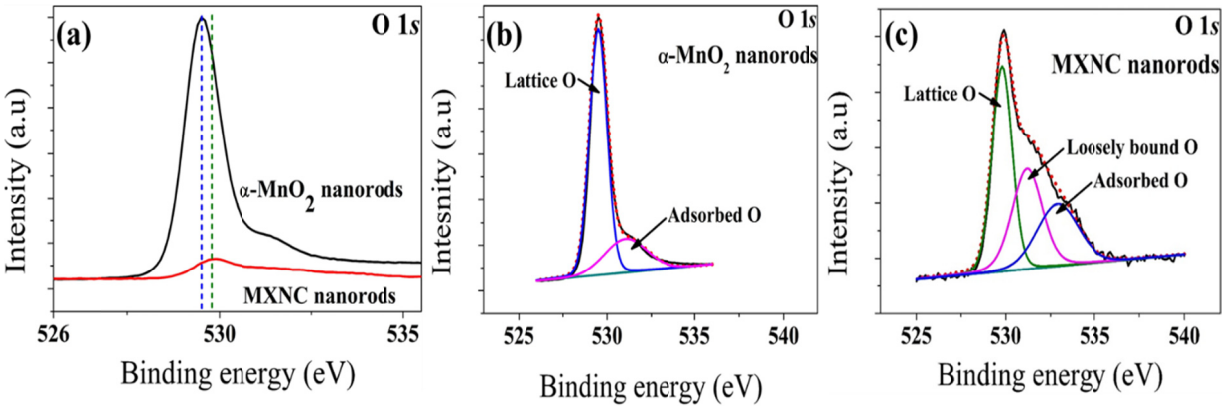

Figure 3. XPS spectra (a) shift comparison of O 1*s* of α-MnO_2 and MXNC nanorods, (b) O 1*s* of α-MnO_2 nanorods, and (c) O 1*s* of MXNC nanorods.

---

was computed from ***Figures 3(b)*** and ***3(c)*** that the ratio of oxygen adsorbed to total oxygen is ~22 and 26% for α-MnO_2 and MXNC nanorods, respectively. The relatively higher ratio in MXNC nanorods indicate that it has higher oxygen vacancies compared to α-MnO_2 nanorods [41], which arise during the reduction of Mn^{4+} to Mn^{3+} and Mn^{2+} under carbonization temperature [42]. The presence of these oxygen vacancies and reduced content of oxygen in MXNC nanorods enhance their oxygen adsorption affinity which increases the ORR rate.

Morphology analysis: The SEM and TEM images of α-MnO_2 nanorods in ***Figures S6(a) and S7(a),*** respectively, show that they are ultralong nanorods with diameter ~30–50 nm. The SAED pattern ***(inset Figure S7(a))*** and FFT ***(inset Figure S7(b))*** can be indexed to (200) and (310) planes of α-MnO_2 crystalline structure that corroborates with the XRD patterns. From HRTEM ***(Figure S7(b))***, the crystal orientation of α-MnO_2 nanorods is revealed to be along (010) direction. It is seen from ***Figures S6(b)*** and ***S7(c)*** that the α-MnO_2@ZIF-67 nanorods exhibit a structure where the α-MnO_2 nanorods have been encapsulated by the ZIF-67 crystals. These

crystals have a diameter of ~ 300 nm. After the carbonization, the MXNC nanorods formed have a carbon shell surrounding the reduced MnO nanorods core ***(Figures S7(d)*** and ***4(a))***. The HRTEM image of MXNC nanorods in ***Figure 4(b)*** reveals a carbon shell layer ~23 nm in thickness. As explained earlier, the carbon shell is an amalgamation of graphitic and disordered carbon. Thus, it can be seen from ***Figure 4(c)*** that there are some defects on the shell which occurred during the carbonization of ZIF-67 crystals. Apart from the role of doped nitrogen and cobalt species in the formation of defects on the carbon shell, it is surmised that the high temperature carbonization is also partially responsible. During the carbonization process under argon gas, the particles undergo diffusive motion. The frictional force imparted due to abrasion against the carbon shell, generate edge defects [43,44]. The formation of MnO core, interstitial $CoMn_2O_4$ at sporadic locations, and oxygen vacancies are observed and their corresponding lattice distances ***(Figure 4(d))*** corroborate with the XRD pattern of MXNC nanorods. The EDX line scan of the MXNC nanorods in ***Figures 4(e) and 4(f)*** proves that the MnO is located at the core, while the MOF-derived N–C exists as the shell.

Electronic conductivity: The voltage versus current graph in ***Figure S8,*** as obtained from the 4-probe conductivity measurement, shows that that the electronic conductivity of the α-MnO_2 nanorod and MXNC nanorod cathodes are 1.22 and 4.25 $S \cdot cm^{-1}$, respectively. The ~4 times higher conductivity of the MXNC nanorod cathode is imparted by the MOF-derived N–C shell, which consists of graphitic and disordered carbon and helps in promoting faster electron transport.

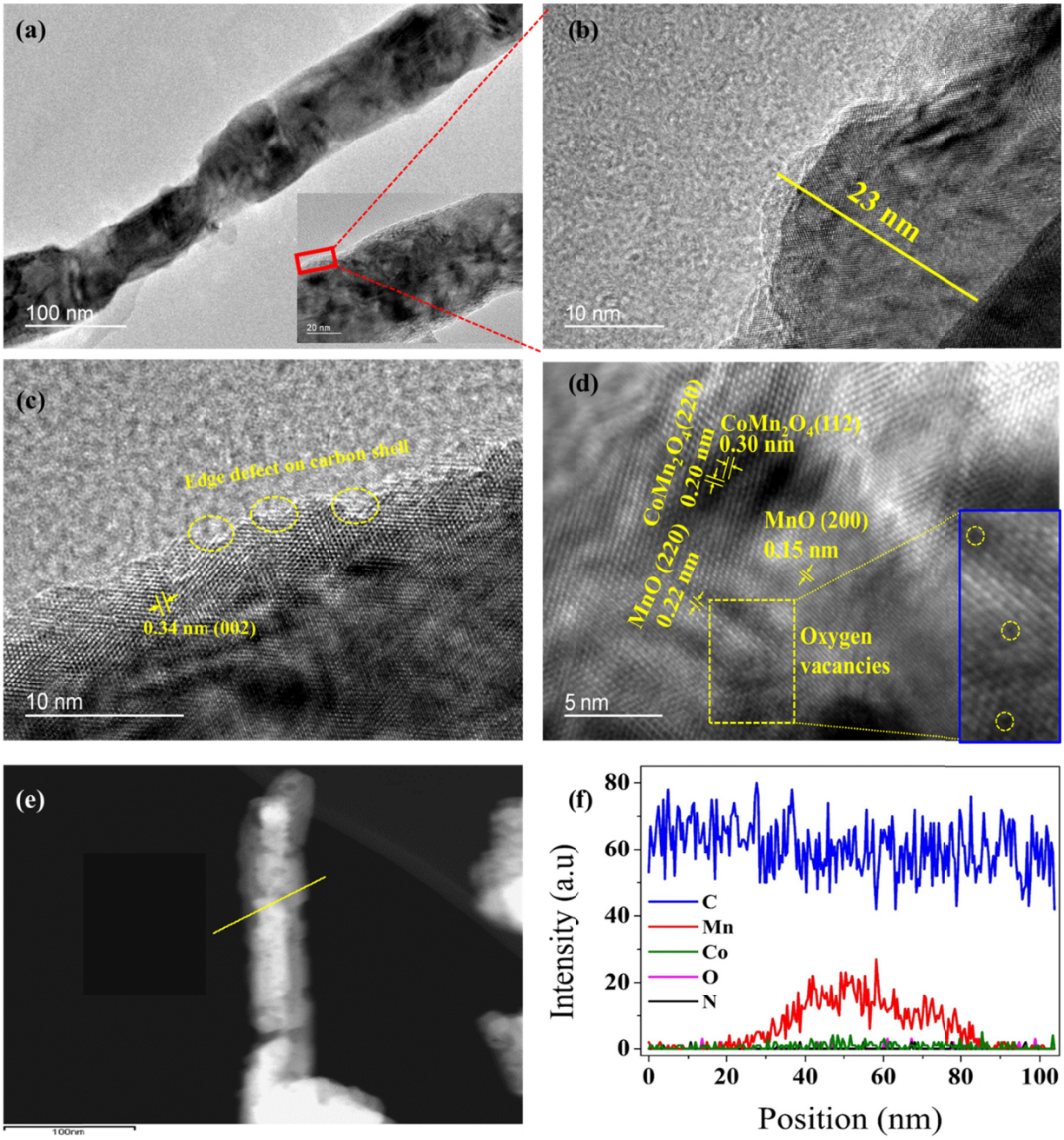

Figure 4. (a) TEM image of a single MXNC nanorod, (b,c,d) HRTEM images of MXNC nanorod, and (e,f) EDX line scan image of MXNC nanorod.

3.2 Electrochemical performance of MXNC nanorod cathode-based LOB cells

The electrochemical characterizations of the MXNC nanorod cathode-based LOB cells are evaluated in this section.

Discharge–charge and rate performance: The full specific discharge and charge capacities of the LOB cells with different cathodes are compared in ***Figure 5(a)***. At a specific current density of 200 $mA \cdot g^{-1}$, the MXNC nanorod cathode-based LOB cell provided a remarkable full specific discharge capacity of 8625 $mAh \cdot g^{-1}$ (~5.17 $mAh \cdot cm^{-2}$). In comparison, the α-MnO_2 nanorod (parental core) and ZIF-67-900 (shell only equivalent) cathode-based LOB cells delivered a full specific discharge capacity of 3144 and 2014 $mAh \cdot g^{-1}$, respectively. The low performance of α-MnO_2 nanorod and ZIF-67-900 cathode-based LOB cells is due to the fact that pristine MnO and CoO by themselves have lower affinity for O_2/OH^- adsorption compared to Co-Mn oxide [45]. Therefore, ZIF-67-900, despite having higher surface area ***(Figure S10)*** than MXNC nanorod delivers lower full specific discharge capacity, proving that the capacity enhancement for MXNC nanorod cathode-based LOB cell is attributed not only to the porous and conductive shell, but also to the electrocatalytic active Mn, Co sites and oxygen vacancies from core and interstitial nanoparticles of MXNC nanorods. The full specific discharge capacity of the MXNC nanorods-650 cathode-based LOB cell is lower due to insufficient graphitization and oxygen vacancies (higher oxygen content than MXNC nanorods) at low carbonization temperature ***(Figures S3(a), and Table 1)***. The increasing trend of discharge and charge polarizations with higher specific current density for MXNC nanorod cathode-based LOB cell ***(Figure 5(b))***, prove that they are stable for ORR–OER reactions. At lower specific current density, the MXNC nanorod cathode-based LOB cell delivered a higher specific discharge capacity due to improved ionic conductivity of Li^+ ions through the porous conductive N–C shell

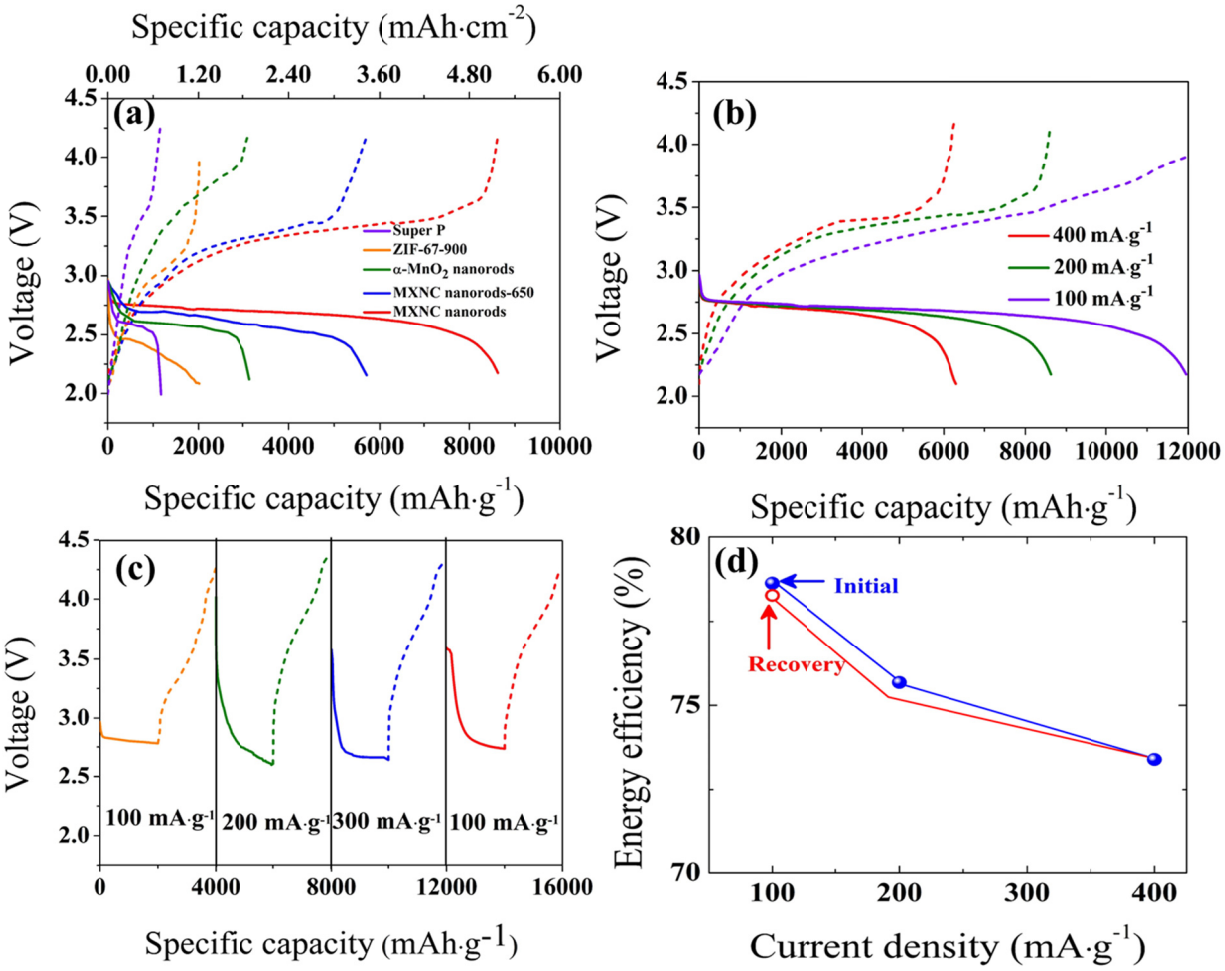

Figure 5. (a) Comparison of first cycle discharge–charge profiles of LOB cells with Super P, ZIF-67-900, α-MnO_2 nanorods, MXNC nanorods-650, and MXNC nanorods as cathodes at full specific discharge capacity and 200 mA·g^{-1} specific current density, (b) comparison of first cycle discharge–charge profiles of MXNC nanorod cathode-based LOB cells at different current densities, (c) rate performance of MXNC nanorod cathode-based LOB cells at limited specific discharge capacity of 2000 mAh·g^{-1}, and (d) corresponding energy efficiencies of MXNC nanorod cathode-based LOB cells at various specific current densities.

network, and the synergism of the active sites comprised of Mn, Co, and oxygen vacancies. With the increasing specific current density, the gradient of oxygen concentration across the cathodes gets elevated, which builds up a diffusion restriction regime across the gas-cathode interface [46]. Despite that, the MXNC nanorod cathode-based LOB cell could deliver up to 6300 $mAh \cdot g^{-1}$ specific discharge capacity at 400 $mA \cdot g^{-1}$, indicating the kinetic stability of ORR–OER on the MXNC nanorod cathodes [47]. The kinetic stability of the MXNC nanorod cathodes is further confirmed from their corresponding LOB cells' rate performances as shown in ***Figures 5(c) and 5(d)***. At a limited specific discharge capacity of 2000 $mAh \cdot g^{-1}$ and increasing the specific current density of 100, 200, and 400 $mA \cdot g^{-1}$, the average discharge voltage continuously decreased as 2.79, 2.76, and 2.74 V accordingly. On the other hand, the corresponding average charging voltage increased with specific current density. The average charging voltages at 100, 200, and 400 $mA \cdot g^{-1}$ were 3.54, 3.64, and 3.73 V accordingly. At a fixed specific discharge capacity and constant specific current density, energy efficiency of a LOB cell is defined as the ratio of average discharge voltage to average charge voltage. Therefore, the energy efficiencies at 100, 200, and 400 $mA \cdot g^{-1}$ are calculated as 78.6, 75.7, and 73.4% accordingly. When the specific current density was set back to 100 $mA \cdot g^{-1}$, the MXNC nanorod cathode-based LOB cell was able to recover with a round trip energy efficiency of 78.3%. The round-trip energy efficiency of MXNC nanorod cathode-based LOB cell at 2000 $mAh \cdot g^{-1}$ limited specific discharge capacity is comparable to RuO_2/NiO, $MnCo_2S_4$ nanosheets, and expensive PtAu/C cathode-based LOB cells [47–49].

Cyclability: To verify the merits of the core@shell structure, the cyclic stability of the MXNC nanorod cathode-based and α-MnO_2 nanorod cathode-based LOB cells were compared at a limited specific discharge capacity of 2000 and 200 $mA \cdot g^{-1}$ specific current density as shown in

Figures 6(a-d). Comparing the first discharge–charge cycles of the LOB cells, it can be observed that the MXNC nanorod cathode reduced the ORR and OER overpotentials by 300 and 110 mV, respectively, compared to α-MnO_2 nanorod cathode, thereby proving the bifunctionality of the MXNC nanorods during discharge–charge. The oxygen vacancies and pyridinic nitrogen content of N–C shell in MXNC nanorod cathode enhance their affinity towards oxygen adsorption [50,51], while the Mn, Co active sites improve the redox kinetics of the ORR–OER, thereby lowering the overpotential. In the subsequent cycles, the discharge voltage decreased, and the charge voltage increased for both the LOB cells. However, the discharge voltage plateau of the MXNC nanorod cathode-based LOB cell showed good consistency till 48th cycle and the voltage dropped till 2.63 V. On the other hand, the discharge voltage plateau for α-MnO_2 nanorod cathode-based LOB cell dropped to 2.16 V by the 10th cycle. The sudden increase in charging voltage from the 1st to 10th cycle in α-MnO_2 nanorod cathode-based LOB cell is attributed to the passivation of the cathode by Li_2CO_3. Generally, the carbon from the electrolyte reacts with the Li_2O_2 to form Li_2CO_3 [52,53]. The decomposition of the Li_2CO_3 require a higher charging voltage than the Li_2O_2, which resulted in the high charging voltage at the 10th and subsequent cycles [48]. The MXNC nanorod cathode-based LOB cell sustained 48 cycles with 100% coulombic efficiency, while the α-MnO_2 nanorod cathode-based LOB cell was stable till 8 cycles, after which the specific discharge capacity and coulombic efficiency started dropping. The high cyclic stability of MXNC nanorod cathode-based LOB cells is attributed to the unique morphology the MXNC nanorods, such as: (i) the synergism of Mn, Co active species and the oxygen vacancies that could efficiently decompose the surface deposited insulated intermediates such as Li_2O_2 [54]; (ii) the N–C shell acted as a shield and prevented the deposition of the

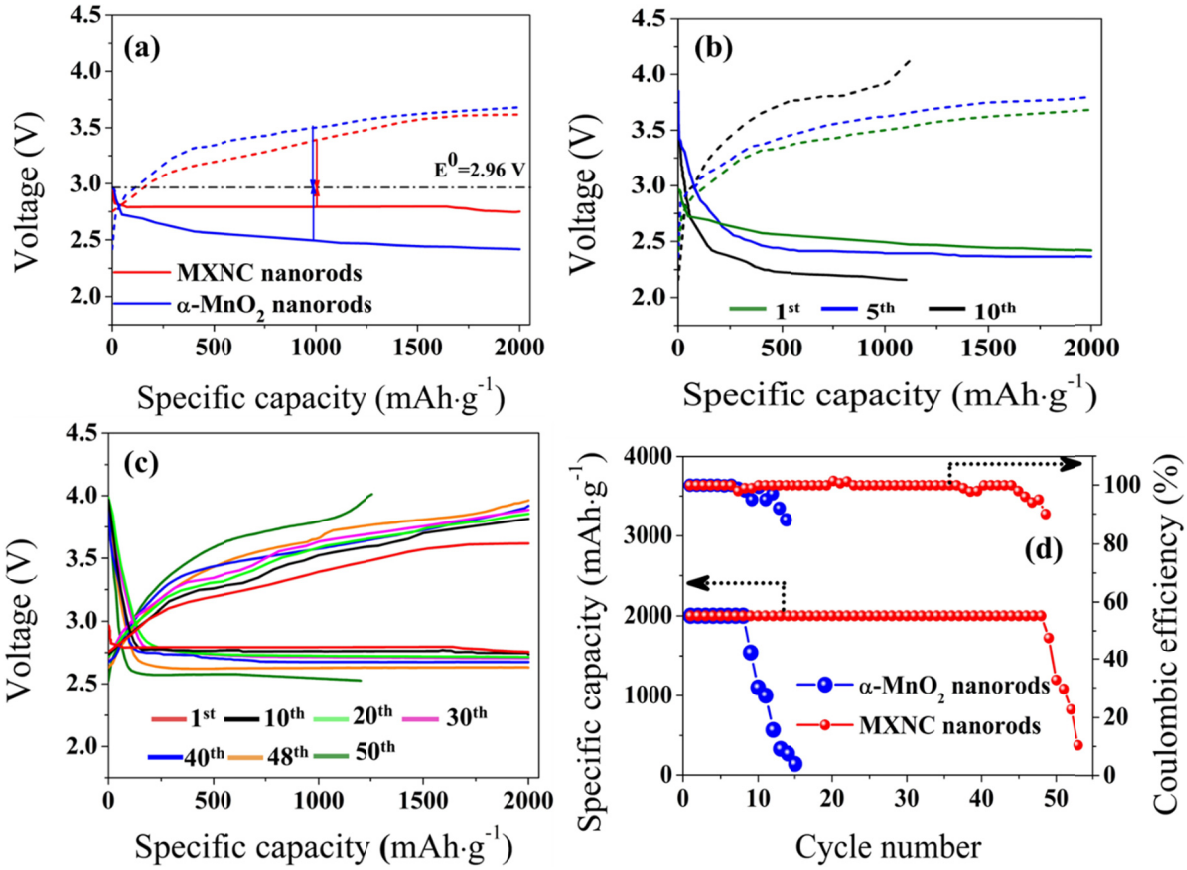

Figure 6. Discharge–charge profiles of LOB cells at 200 $mA \cdot g^{-1}$ specific current density and limited specific discharge capacity of 2000 $mAh \cdot g^{-1}$: (a) first cycle of α-MnO_2 nanorods and MXNC nanorod cathode-based LOB cells, (b) various cycles of α-MnO_2 nanorod cathode-based LOB cell, (c) various cycles of MXNC nanorod cathode-based LOB cell, and (d) cyclic performance and coulombic efficiencies of α-MnO_2 nanorods and MXNC nanorod cathode-based LOB cells at 200 $mA \cdot g^{-1}$ specific current density and limited specific discharge capacity of 2000 $mAh \cdot g^{-1}$.

---

insulating Li_2O_2 side products directly on the MnO core and interstitial $CoMn_2O_4$ active species; and (iii) the porous N–C shell could accommodate the Li_2O_2 and prevent the pore clogging.

Electrochemical impedance spectroscopy (EIS): The electrochemical kinetics of MXNC nanorods and α-MnO_2 nanorods as cathodes for LOB cells were compared by CV in the potential range of 2–4.5 V ***(Figure 7(a))***. In the absence of oxygen, MXNC nanorod cathodes showed almost no ORR–OER activities. However, in the presence of oxygen, the specific current density

of MXNC nanorod cathodes, in both ORR and OER regions surpassed that of the α-MnO_2 nanorod cathodes. The ORR and OER onset potentials for MXNC nanorods were higher and lower respectively compared to α-MnO_2 nanorods. The high Mn^{4+} content in α-MnO_2 nanorod improves the ORR but inhibits the surface OH^- oxidation and lowers the OER rate [55]. Their poor electrical conductivity further impedes the electrochemical performance. On the other hand, Mn^{2+} and Mn^{3+} in conductive MXNC nanorods are favourable for exchange of oxygen atoms, stabilizing the O_2 adsorbates, and improving rates of electron transfer during ORR. This results in reducing the overpotential [27,52,55]. The addition of Co increases the Mn–O covalency, thus strengthening the Mn–O bond, and promoting redox reactions [56]. The multivalent Co and Mn in $CoMn_2O_4$ decoration has low oxygen binding ability, hence conducive to the OER [14,57]. Additionally, the oxygen vacancies present in MXNC nanorods act beneficially towards both ORR and OER by adsorbing O_2 and stabilizing the OER intermediates respectively [34,54]. The presence of large number of active electrocatalytic sites in form of MnO, $CoMn_2O_4$, and oxygen vacancies in the MXNC nanorods reduce the activation barrier for ORR–OER. Due to the absence of multivalent Co ions and oxygen vacancies, the α-MnO_2 nanorods show higher OER onset potential and smaller peak. The sluggish OER performance in α-MnO_2 nanorods results in incomplete decomposition of Li_2O_2 and eventually failure of the battery after 8^{th} cycle. The high porosity of the N–C shell in MXNC nanorods exposes and stabilizes the metal active sites as well as improves the mass transport for intermediates. The conductivity of the N–C shell

enhances the electron transport through the 1D core in MXNC nanorods. Such synergistic effect has been observed in various metal-nitrogen-carbon (M–N–C) electrocatalysts such as: Co−Ni/N–C or Co_3O_4/MnO_2-CNTs used in zinc-air battery, CoMn2O4/N–CNT/3D graphene for aluminium-air battery, Co–Fe binary alloy embedded bimetallic organic frameworks used in alkaline fuel cell, and Fe–N–C electrocatalyst for proton exchange membrane fuel cells [45,51,58–60]. It is to be noted that MXNC nanorod cathodes feature a second small peak at 4.34 V in the OER regime owing to the stepwise decomposition of Li_2O_2. Possibly, the bulk particle-type Li_2O_2 deposits on the cathode was decomposed at low potentials (3.24 V) through electron tunnelling, while the film-type Li_2O_2 decomposed at high potentials through polaron hopping [61,62]. The EIS spectra of α-MnO_2 nanorods and MXNC nanorod cathodes in ***Figures 7(b) and 7(c)*** agree with the galvanostatic results described previously and reflect the electrochemical superiority of the latter. The ZView software was used to fit the impedance spectra to generate the equivalent circuit ***(inset in Figure 7(c))***. The ionic resistance, R_s is imparted by the electrolyte. R_{ct} is the resistance against charge transfer process at the anode/electrolyte and the electrolyte/cathode interface. CPEdl is the constant phase element due to the double layer capacitance. Z_w is the Warburg impedance arising due to the resistance against Li^+ ion diffusion [34,46]. The initial resistance parameters, R_s and R_{ct} of MXNC nanorod cathodes before cycles were lower compared to the α-MnO_2 nanorod cathodes ***(Table S2)***. For the α-MnO_2 nanorod cathodes, R_{ct} rapidly increased from the 1^{st} to the 10^{th} cycle due to the increased thickness of the insulating Li_2O_2 or Li_2CO_3 layer at the electrolyte/cathode interface [63]. This corroborates the increase in overpotential from the 1^{st} to the 10^{th} cycle as in ***Figure 6(b)***. The R_{ct} increased significantly for both the cathodes after the first discharge. This was due to the build-up of the

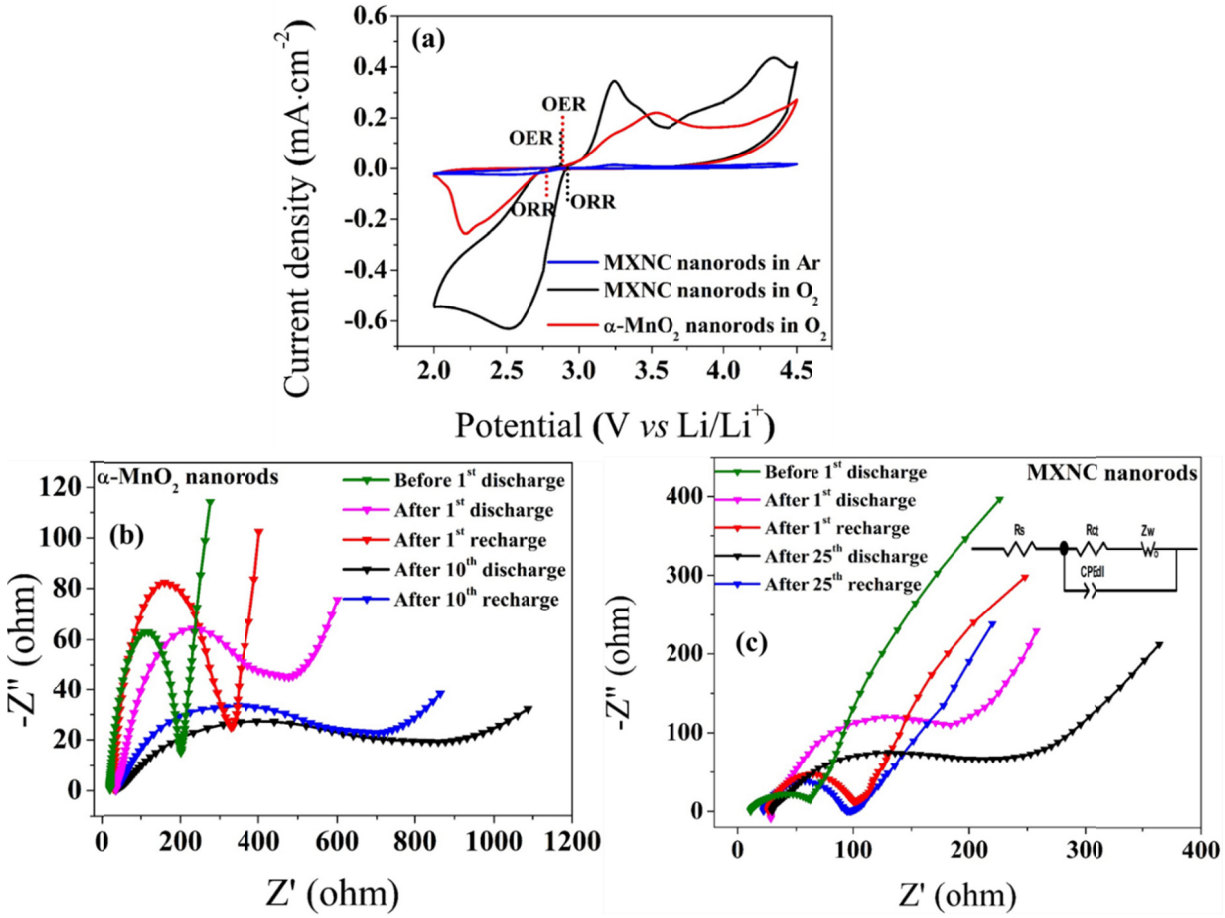

Figure 7. (a) CV curves, (b-c) Nyquist plots of α-MnO_2 nanorods and MXNC nanorod cathode-based LOB cells, and (inset in c) equivalent circuit fitted with the Nyquist plots.

Li_2O_2 side products. However, due to the effective redox reactions, after recharging, MXNC nanorod cathodes recovered their state and exhibited R_{ct} of ~72.69 Ω. In contrast, α-MnO_2 nanorod cathodes showed a higher R_{ct} after recharging due to poor redox reaction over limited electrocatalytic sites. Owing to the high stability of the MXNC nanorod cathodes in contact with the electrolyte, its resistance parameters after 25 cycles, was lower, than, α-MnO_2 nanorod cathodes in the 10^{th} cycle. Hence, the α-MnO_2 nanorod cathodes failed after 8^{th} cycle. Since R_{ct} is the dominant change in the discharged cathodes, it can be presumed that the loss of capacity and

death of the LOB cells mainly occurred due to poor charge transport across the deposited Li_2O_2 during OER [63]. The CPEdl of the MXNC nanorod cathodes was higher than the α-MnO_2 nanorod cathodes signifying the presence of higher number of electrocatalytic active sites that drive the ORR–OER reactions and their high capability to store charges in hierarchical pores of the conductive shell during the discharge–charge cycles. The CPEdl increased with charging for both the cathodes reflecting the process of oxidation of Li_2O_2 during OER. The faster OER kinetics on the Mn, Co sites of MXNC nanorod cathodes resulted in a significantly higher CPEdl after the first recharge. Further, the CPEdl of α-MnO_2 nanorod cathodes after the 10^{th} recharge was lower than the pristine cathode indicating that the insulating Li_2O_2 deposit had not been completely decomposed by the Mn active sites [64]. The passivation of the active sites of α-MnO_2 nanorod cathodes by Li_2O_2 decreased the specific discharge capacity at the 10^{th} cycle ***(Figure 5(b))***. The morphological attributes of high surface area and short diffusion paths offered by the hierarchical pores of MXNC nanorod cathodes facilitated the electrolyte permeability. The lower Z_w for MXNC nanorod cathodes indicated the dominant mass transport and faster diffusion of Li^+ ions across the electrolyte/cathode interface [48]. Z_w increased during discharge due to the pore blocking by the Li_2O_2 and the reduced Li^+ ion diffusivity.

Post-mortem characterizations and proposed mechanism of ORR–OER in LOB cells: To evaluate the reversibility of the formation and decomposition of Li_2O_2 on the discharged and recharged MXNC nanorod cathodes respectively, we conducted *ex-situ* XRD, Raman spectroscopy, and SEM on the discharged and recharged cathodes. As shown in ***Figure S9(a)***, the peak at 790 cm^{-1} indicates the formation of Li_2O_2 side products on the discharged MXNC nanorod cathodes [65]. However, in the subsequent recharged MXNC nanorod cathodes, the

Li_2O_2 peak is absent. Similarly, the XRD patterns of the discharged MXNC nanorod cathodes (both 25th and 50th cycles) in ***Figure S9(b)*** showed the presence of Li_2O_2 (JCPDS-09-0355), which decomposed on recharging. It should be noted that the discharged MXNC nanorod cathode at the end of 50th cycle showed an extra peak of Li_2CO_3, both in XRD pattern and Raman spectrum. Due to the reduced stability of the MXNC nanorod cathodes in contact with the electrolyte at the end of 50th cycle, the decomposed electrolyte reacted with the surface species of the cathode and the Li_2O_2 to form irreversible Li_2CO_3 [66]. The particle-type Li_2O_2 formation could be observed from the SEM after the 25th discharge, which disappeared after the recharge. Interestingly, a film-type Li_2O_2 was formed at the end of the 50th discharge cycle. The gradual deposition of irreversible Li_2CO_3 and film-type Li_2O_2 resulted in the drastic drop of the specific discharge capacity and loss of reversibility in MXNC nanorod cathode-based LOB cells at the end of 50th discharge cycle [65].

In this regard, it is important to analyse the reaction mechanisms that underwent in the LOB cells during the discharge–charge reactions and the consequent formation of different Li_2O_2 morphologies. The ORR–OER reactions generally follow the below pathways [67–69]:

$$Li^+_{(sol)} + e^- + O_{2\,(sol)} \rightarrow Li^+_{(sol)} + O_2^-{}_{(sol)} \qquad \textit{Equation 1}$$

$$LiO_2^* \rightarrow Li^+_{(sol)} + O_{2\,(sol)} + \text{ion pairs+ higher aggregates} \qquad \textit{Equation 2}$$

$$2(Li^+_{(sol)} + O_2^-{}_{(sol)}) \rightarrow Li_2O_2 + O_2 \qquad \textit{Equation 3}$$

$$2Li^+_{(sol)} + O_2^-{}_{(sol)} + e^- \rightarrow LiO_2^* + Li^+ + e^- \rightarrow Li_2O_2 \qquad \textit{Equation 4}$$

During discharge, the Li^+ ions diffused through the porous N–C shell and migrated towards the core and interstitial active sites composed of Mn, Co, and oxygen vacancies. Due to the fast

electron transfer between multivalent Mn, Co ions and N–C shell [70], the formation of solvated LiO_2^* intermediates in electrolyte was favoured [71]. The oxygen vacancies combined the O_2 with solvated LiO_2^* and following a disproportionation reaction gave rise to Li_2O_2 particles ***(Equations 1–3)*** in the 25th discharge cycle ***(Figure 8(b))***. After the 25th recharge, oxidation of Li_2O_2 was evident from the free surface of MXNC nanorod cathodes as depicted in ***Figure 8(c)***, which was comparable to the initial state of the cathodes ***(Figure 8(a))***. This is attributed to the large number of active sites and facilitated mass transport through the hierarchically porous structure of MXNC nanorods that accelerated the decomposition of Li_2O_2 at low overpotential. However, at the 50th cycle, the MXNC nanorod cathode-based LOB cell failed and their corresponding overpotential was high as shown in ***Figures 6(c) and 6(d)***. It is presumed that with increasing cycles, some active sites were passivated, and the undecomposed Li_2O_2 was accommodated in the N–C shell. This reduced the porosity of the N–C shell, and the diffusion of Li^+ ions and electron transfer through the core diminished, hence, the LiO_2* was adsorbed on the surface-exposed defect sites of the N–C shell. The high concentration of adsorbed LiO_2*could not be efficiently solvated by the electrolyte, hence the LiO_2* disproportionated a second time via surface adsorption pathway ***(Equation 4)*** to form a film-type Li_2O_2 [71] as shown in ***Figure 8(d)***. The film-type Li_2O_2 deposition drastically increased the charge transfer resistance [69]. Additionally, the carbon from the electrolyte reacted with the Li_2O_2 to form Li_2CO_3, that fuelled the loss of reversibility and death of the cell [53,69].

The OER occurring during the recharge oxidized the Li_2O_2 via the following pathways [62]:

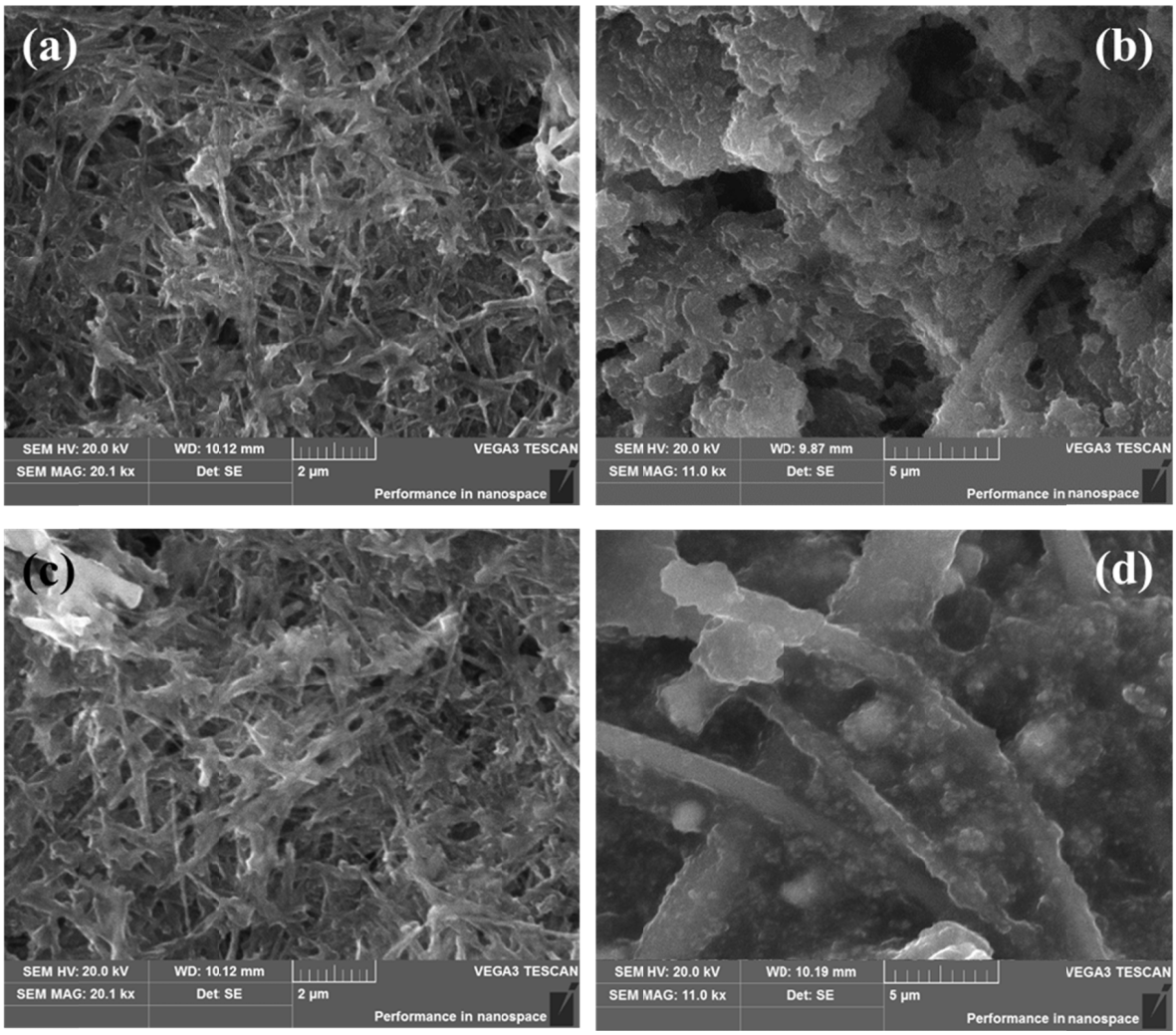

Figure 8. SEM images of MXNC nanorod cathodes (a) before 1st discharge, (b) after 25th discharge, (c) after 25th recharge, and (d) after 50th discharge.

$$Li_2O_2 \rightarrow Li^+ + e^- + LiO_{2\,(sol)} \qquad \textit{Equation 5}$$

$$Li_2O_2 \rightarrow 2Li^+ + 2\,e^- + O_2 \qquad \textit{Equation 6}$$

Here, the particle- and film-type Li_2O_2 deposits decompose through one ***(Equation 5)*** and two electron transfer ***(Equation 6)*** respectively [62]. The interstitial tetragonal $CoMn_2O_4$ nanoparticle

interstitial decoration and oxygen vacancies accelerate the decomposition of Li_2O_2, thus proving the bifunctionality of the MXNC nanorods [72].

The above results prove that the active sites comprised of Mn, Co, and oxygen vacancies act as bifunctional electrocatalytic sites for the ORR–OER [73,74] in MXNC nanorod cathodes, while the N–C shell provide the necessary conductivity and protect the core electrocatalytic sites from passivation by accommodating the Li_2O_2 deposits. The improvement in the ORR–OER due to the modified morphology and bifunctionality of MXNC nanorods is depicted from the CV curve with favourable onset potentials and high specific current density. The pyridinic nitrogen content of the carbon shell enhance the oxygen adsorption [74], while the MnO and interstitial $CoMn_2O_4$ nanoparticles with mixed valence states stabilize the electrocatalytic sites and accelerate the ORR–OER [72]. Oxygen vacancies promote both ORR and OER by improving the migration of Li^+ ions and electrons, as well as, acting as active sites for binding to oxygen and Li_2O_2 [57]. The co-existence of core and interstitial active sites composed of oxygen vacancies and multivalent Mn, Co impart bifunctionality that favour both ORR and OER [14,34,42,54]. This corroborates with various M–N–C type electrocatalysts [45,51,58–60]. Further *in-situ* investigations are required to distinguish the exact electrocatalytic sites responsible for the specific reactions during discharging and charging. The high specific surface area and hierarchical porosity of the MXNC nanorods enhance the diffusion of the Li^+ ions and oxygen, while the conductive N–C shell promote electrical conductivity. These features led to lower overpotential and higher cyclability of the MXNC nanorod cathode-based LOB cell. However, the incoming oxygen is also responsible for its reaction with the Li^+ ions to form the side products: Li_2O_2 and Li_2CO_3.

Overall, the above proposed ORR–OER mechanism can support the different morphologies of Li_2O_2 depositions on the cathode surface, the discharge–charge profiles, CV, and EIS curves generated from the LOB cells with MXNC nanorod cathodes.

4. Conclusions

We have successfully synthesized core@shell-structured, hierarchically porous MnO/$CoMn_2O_4$@N–C (MXNC) nanorods with interstitial $CoMn_2O_4$ nanoparticle decorations, as a bifunctional electrocatalyst for high-performance cathodes in LOBs. The one-step carbonization process of the α-MnO_2@ZIF-67 MOF, have led to the formation a nanoarchitecture consisting of a protective N–C shell over the core MnO nanorods and interstitial $CoMn_2O_4$ nanoparticles. When used as cathodes in LOB cells, the MXNC nanorods have showed ~6 times higher cyclability (48 cycles) than the α-MnO_2 nanorods at a limited specific discharge capacity of 2000 $mAh \cdot g^{-1}$ and specific current density of 200 $mA \cdot g^{-1}$. The MXNC nanorod cathode-based LOB cells have exhibited a full specific discharge capacity of 8625 $mAh \cdot g^{-1}$ at 200 $mA \cdot g^{-1}$ specific current density, that is ~ 2.7 times compared to α-MnO_2 nanorods counterparts. The electrochemical kinetic stability of the MXNC nanorod cathode is seen from their round-trip energy efficiency of 78.3%, which is comparable to RuO_2/NiO, $MnCo_2S_4$ nanosheets, and expensive PtAu/C cathodes. Correlating the structural and electrochemical characterizations of MXNC nanorods, it has been deduced that the high specific discharge capacity and low overpotential of the LOB cells are a result of the increased number of bifunctional electrocatalytic sites imparted by the MnO core, interstitial multivalent $CoMn_2O_4$ nanoparticle decoration, and oxygen vacancies. The MOF-derived porous conductive N–C shell promoted the electron migration and acted as a protective barrier over the core active sites

against Li_2O_2 depositions, thus improving the cyclability. The bifunctional actives sites and core@shell structure of MXNC nanorods have also influenced the LiO_2* solvation and resulted in formation of particle- and film-type Li_2O_2 deposits on the cathode surface. These results signify that careful tailoring of MOF-derived shells over transition metal oxides is a promising strategy to improve the bifunctionality, porosity, and conductivity of inexpensive cathodes for non-aqueous LOBs. Since MOF is tunable, therefore, this approach may be extended to fine-tune the composition and morphology of the interstitial nanoparticles for applications in other type of air-batteries and supercapacitors. Further investigations on the electrolyte would shed new lights on the solubility of intermediate LiO_2* and prevention of Li_2O_2 growth and cell death.

Conflicts of interest

There are no conflicts to declare.

Acknowledgements

This work was supported by the Research Grants Council of the HKSAR Government (Grant Nos. 15217917 and R5020-18) and the Innovation and Technology Commission of the HKSAR Government to the Hong Kong Branch of National Rail Transit Electrification and Automation Engineering Technology Research Center (Grant No. K-BBY1). The authors were grateful to Ms. Alorika Chatterjee at IACS, Kolkata, India for the assistance in the Rietveld refinement of the XRD patterns.

Electronic Supplementary Information

Figure S1- Assembling of LOB cell using EQ-STC-Li-air split cell; Figure S2 (a–b)- Thermogravimetric (TG) curves at 10 °C·min^{-1} heating rate for (a) α-MnO_2@ZIF-67 nanorods obtained in nitrogen flow and (b) MXNC nanorods obtained in air flow; Figure S3 (a–d)- (a) XRD patterns with Rietveld refinement of α-MnO_2 nanorods, (b) crystal structure of α-MnO_2 nanorods, (c) XRD patterns with Rietveld refinement of ZIF-67, and (d) crystal structure of ZIF-67; Table S1- Rietveld refinement parameters; Figure S4- Pore size distribution of MXNC and α-MnO_2 nanorods; Figure S5- Overall XPS spectra of MXNC and α-MnO_2 nanorods; Figure S6 (a–b)- SEM images of (a) α-MnO_2 and (b) α-MnO_2@ZIF-67 nanorods; Figure S7 (a–d)- (a) TEM image and SAED pattern (inset) of α-MnO_2 nanorods, (b) HRTEM image and FFT pattern (inset) of α-MnO_2 nanorods, (c) TEM image of α-MnO_2@ZIF-67 nanorods, and (d) TEM image of MXNC nanorods; Table S2- Resistance parameters as calculated from equivalent circuit; Figure S8- Voltage versus current profiles of α-MnO_2 nanorod and MXNC nanorod cathodes; Figure S9 (a–b)- (a) Raman spectroscopy and (b) XRD patterns of MXNC nanorod cathodes before discharge, after 25th discharge, after 25th recharge, after 50th discharge, and after 50th recharge. Figure S10- N_2 adsorption-desorption isotherms of ZIF-67-900.

References

[1] N. Imanishi, O. Yamamoto, Rechargeable lithium-air batteries: Characteristics and prospects, Mater. Today. 17 (2014) 24–30. doi:10.1016/j.mattod.2013.12.004.

[2] P.G. Bruce, S.A. Freunberger, L.J. Hardwick, J.-M. Tarascon, Li–O2 and Li–S batteries with high energy storage, Nat. Mater. 11 (2011) 172–172. doi:10.1038/nmat3237.

[3] A. Eftekhari, B. Ramanujam, In pursuit of catalytic cathodes for lithium–oxygen batteries, J. Mater. Chem. A. 5 (2017) 7710–7731. doi:10.1039/C7TA01124E.

[4] Z. Ma, G. Shao, Y. Fan, G. Wang, J. Song, D. Shen, Construction of Hierarchical α-MnO2Nanowires@Ultrathin δ-MnO2Nanosheets Core-Shell Nanostructure with Excellent Cycling Stability for High-Power Asymmetric Supercapacitor Electrodes, ACS Appl. Mater. Interfaces. 8 (2016) 9050–9058. doi:10.1021/acsami.5b11300.

[5] A. Débart, A.J. Paterson, J. Bao, P.G. Bruce, α-MnO2 nanowires: A catalyst for the O2 electrode in rechargeable lithium batteries, Angew. Chemie - Int. Ed. 47 (2008) 4521–4524. doi:10.1002/anie.200705648.

[6] V. Giordani, S.A. Freunberger, P.G. Bruce, J.-M. Tarascon, D. Larcher, H[sub 2]O[sub 2] Decomposition Reaction as Selecting Tool for Catalysts in Li–O[sub 2] Cells, Electrochem. Solid-State Lett. 13 (2010) A180. doi:10.1149/1.3494045.

[7] B. Liu, Y. Sun, L. Liu, S. Xu, X. Yan, Advances in Manganese-Based Oxides Cathodic Electrocatalysts for Li-Air Batteries, Adv. Funct. Mater. 1704973 (2018) 1–34. doi:10.1002/adfm.201704973.

[8] W. Bin Luo, S.L. Chou, J.Z. Wang, Y.C. Zhai, H.K. Liu, A facile approach to synthesize

stable CNTs@MnO electrocatalyst for high energy lithium oxygen batteries, Sci. Rep. 5 (2015). doi:10.1038/srep08012.

[9] H.W. Park, D.U. Lee, L.F. Nazar, Z. Chen, Oxygen Reduction Reaction Using MnO2 Nanotubes/Nitrogen-Doped Exfoliated Graphene Hybrid Catalyst for Li-O2 Battery Applications, J. Electrochem. Soc. 160 (2012) A344–A350. doi:10.1149/2.086302jes.

[10] X. Zhai, W. Yang, M. Li, G. Lv, J. Liu, X. Zhang, Noncovalent hybrid of CoMn2O4spinel nanocrystals and poly (diallyldimethylammonium chloride) functionalized carbon nanotubes as efficient electrocatalysts for oxygen reduction reaction, Carbon N. Y. 65 (2013) 277–286. doi:10.1016/j.carbon.2013.08.026.

[11] L. Wang, X. Zhao, Y. Lu, M. Xu, D. Zhang, R.S. Ruoff, K.J. Stevenson, J.B. Goodenough, CoMn2O4 Spinel Nanoparticles Grown on Graphene as Bifunctional Catalyst for Lithium-Air Batteries, J. Electrochem. Soc. 158 (2011) A1379. doi:10.1149/2.068112jes.

[12] S. Ma, L. Sun, L. Cong, X. Gao, C. Yao, X. Guo, L. Tai, P. Mei, Y. Zeng, H. Xie, R. Wang, Multiporous MnCo2O4microspheres as an efficient bifunctional catalyst for nonaqueous Li-O2batteries, J. Phys. Chem. C. 117 (2013) 25890–25897. doi:10.1021/jp407576q.

[13] C.W.A. Chan, A.H. Mahadi, M.M.-J. Li, E.C. Corbos, C. Tang, G. Jones, W.C.H. Kuo, J. Cookson, C.M. Brown, P.T. Bishop, S.C.E. Tsang, Interstitial modification of palladium nanoparticles with boron atoms as a green catalyst for selective hydrogenation., Nat. Commun. (2014). doi:10.1038/ncomms6787.

[14] J. Zhang, L. Wang, L. Xu, X. Ge, X. Zhao, M. Lai, Z. Liu, W. Chen, Porous cobalt-

manganese oxide nanocubes derived from metal organic frameworks as a cathode catalyst for rechargeable Li-O2batteries, Nanoscale. 7 (2015) 720–726. doi:10.1039/c4nr05865h.

[15] W. Yin, Y. Shen, F. Zou, X. Hu, B. Chi, Y. Huang, Metal-organic framework derived ZnO/ZnFe2O4/C nanocages as stable cathode material for reversible lithium-oxygen batteries, ACS Appl. Mater. Interfaces. 7 (2015) 4947–4954. doi:10.1021/am509143t.

[16] Z. Hu, Z. Zhang, Z. Li, M. Dou, F. Wang, One-Step Conversion from Core-Shell Metal-Organic Framework Materials to Cobalt and Nitrogen Codoped Carbon Nanopolyhedra with Hierarchically Porous Structure for Highly Efficient Oxygen Reduction, ACS Appl. Mater. Interfaces. (2017). doi:10.1021/acsami.7b00736.

[17] G. Xu, P. Nie, H. Dou, B. Ding, L. Li, X. Zhang, Exploring metal organic frameworks for energy storage in batteries and supercapacitors, Mater. Today. 20 (2017) 191–209. doi:10.1016/j.mattod.2016.10.003.

[18] Y. Lu, H. Zhu, W.J. Wang, B.G. Li, S. Zhu, Rapid collection and re-dispersion of MOF particles by a simple and versatile method using a thermo-responsive polymer, RSC Adv. (2016). doi:10.1039/c6ra13938h.

[19] J. Jia, P. Zhang, L. Chen, The effect of morphology of α-MnO2on catalytic decomposition of gaseous ozone, Catal. Sci. Technol. 6 (2016) 5841–5847. doi:10.1039/c6cy00301j.

[20] W. Li, X. Cui, R. Zeng, G. Du, Z. Sun, R. Zheng, S.P. Ringer, S.X. Dou, Performance modulation of α-MnO2 nanowires by crystal facet engineering, Sci. Rep. 5 (2015) 8987. doi:10.1038/srep08987.

[21] A.F. Gross, E. Sherman, J.J. Vajo, Aqueous room temperature synthesis of cobalt and zinc

sodalite zeolitic imidizolate frameworks, Dalt. Trans. 41 (2012) 5458–5460. doi:10.1039/c2dt30174a.

[22] J. Tang, R.R. Salunkhe, H. Zhang, V. Malgras, T. Ahamad, S.M. Alshehri, N. Kobayashi, S. Tominaka, Y. Ide, J.H. Kim, Y. Yamauchi, Bimetallic metal-organic frameworks for controlled catalytic graphitization of nanoporous carbons, Sci. Rep. 6 (2016) 3–4. doi:10.1038/srep30295.

[23] M. Zhong, D. Yang, C. Xie, Z. Zhang, Z. Zhou, X.H. Bu, Yolk–Shell MnO@ZnMn2O4/N–C Nanorods Derived from α-MnO2/ZIF-8 as Anode Materials for Lithium Ion Batteries, Small. 12 (2016) 5564–5571. doi:10.1002/smll.201601959.

[24] W. Xia, J. Zhu, W. Guo, L. An, D. Xia, R. Zou, Well-defined carbon polyhedrons prepared from nano metal-organic frameworks for oxygen reduction, J. Mater. Chem. A. 2 (2014) 11606–11613. doi:10.1039/c4ta01656d.

[25] X. Wang, J. Zhou, H. Fu, W. Li, X. Fan, G. Xin, J. Zheng, X. Li, MOF derived catalysts for electrochemical oxygen reduction, J. Mater. Chem. A. 2 (2014) 14064–14070. doi:10.1039/c4ta01506a.

[26] K. Song, J. Jung, Y.U. Heo, Y.C. Lee, K. Cho, Y.M. Kang, α-MnO2nanowire catalysts with ultra-high capacity and extremely low overpotential in lithium-air batteries through tailored surface arrangement, Phys. Chem. Chem. Phys. 15 (2013) 20075–20079. doi:10.1039/c3cp53754d.

[27] J.A. Vigil, T.N. Lambert, J. Duay, C.J. Delker, T.E. Beechem, B.S. Swartzentruber, Nanoscale Carbon Modified α-MnO2Nanowires: Highly Active and Stable Oxygen Reduction Electrocatalysts with Low Carbon Content, ACS Appl. Mater. Interfaces. 10

(2018) 2040–2050. doi:10.1021/acsami.7b16576.

[28] Z. Meng, H. Cai, H. Tang, Bimetallic Zeolitic imidazolate framework-derived porous carbon as efficient bifunctional electrocatalysts for Zn-air battery, Int. J. Electrochem. Sci. 13 (2018) 5788–5797. doi:10.20964/2018.06.20.

[29] J. Wang, L. Liu, S. Chou, H. Liu, J. Wang, A 3D porous nitrogen-doped carbon-nanofiber-supported palladium composite as an efficient catalytic cathode for lithium–oxygen batteries, J. Mater. Chem. A. 5 (2017) 1462–1471. doi:10.1039/C6TA07050G.

[30] X. Wang, Y. Li, Nanoporous carbons derived from MOFs as metal-free catalysts for selective aerobic oxidations, J. Mater. Chem. A. 4 (2016) 5247–5257. doi:10.1039/c6ta00324a.

[31] Z. Tang, H. Kang, Z. Shen, B. Guo, L. Zhang, D. Jia, Grafting of polyester onto graphene for electrically and thermally conductive composites, Macromolecules. 45 (2012) 3444–3451. doi:10.1021/ma300450t.

[32] J. Fu, C. Wang, Z. Feng, R. Zhang, Ultralong α-MnO2 Nanowires Capable of Catalytically Degrading Methylene Blue at Low Temperature, Catal. Letters. 148 (2018) 2822–2829. doi:10.1007/s10562-018-2454-9.

[33] Z. Ren, J. Li, Y. Ren, S. Wang, Y. Qiu, J. Yu, Large-scale synthesis of hybrid metal oxides through metal redox mechanism for high-performance pseudocapacitors, Sci. Rep. 6 (2016) 1–10. doi:10.1038/srep20021.

[34] Z. Sadighi, J. Huang, L. Qin, S. Yao, J. Cui, J.K. Kim, Positive role of oxygen vacancy in electrochemical performance of CoMn2O4cathodes for Li-O2batteries, J. Power Sources.

365 (2017) 134–147. doi:10.1016/j.jpowsour.2017.08.081.

[35] H. Bordeneuve, C. Tenailleau, S. Guillemet-Fritsch, R. Smith, E. Suard, A. Rousset, Structural variations and cation distributions in Mn3-xCoxO4($0 \leq x \leq 3$) dense ceramics using neutron diffraction data, Solid State Sci. 12 (2010) 379–386. doi:10.1016/j.solidstatesciences.2009.11.018.

[36] J. Zhang, C. Li, Z. Peng, Y. Liu, J. Zhang, Z. Liu, D. Li, 3D free-standing nitrogen-doped reduced graphene oxide aerogel as anode material for sodium ion batteries with enhanced sodium storage, Sci. Rep. 7 (2017) 1–7. doi:10.1038/s41598-017-04958-1.

[37] P. Zhang, F. Sun, Z. Xiang, Z. Shen, J. Yun, D. Cao, ZIF-derived in situ nitrogen-doped porous carbons as efficient metal-free electrocatalysts for oxygen reduction reaction, Energy Environ. Sci. 7 (2014) 442–450. doi:10.1039/C3EE42799D.

[38] Z. Li, Y. Wang, Y. Chen, M. Wu, Controllable growth of MnO:Xdual-nanocrystals on N-doped graphene as lithium-ion battery anode, RSC Adv. 7 (2017) 6396–6402. doi:10.1039/c6ra27297e.

[39] L.R. Shah, B. Ali, H. Zhu, W.G. Wang, Y.Q. Song, H.W. Zhang, S.I. Shah, J.Q. Xiao, Detailed study on the role of oxygen vacancies in structural, magnetic and transport behavior of magnetic insulator: Co-CeO2, J. Phys. Condens. Matter. 21 (2009) 1–9. doi:10.1088/0953-8984/21/48/486004.

[40] S. Rahimnejad, J.H. He, W. Chen, K. Wu, G.Q. Xu, Tuning the electronic and structural properties of WO3 nanocrystals by varying transition metal tungstate precursors, RSC Adv. 4 (2014) 62423–62429. doi:10.1039/c4ra10650d.

[41] D. Jampaiah, V.K. Velisoju, P. Venkataswamy, V.E. Coyle, A. Nafady, B.M. Reddy, S.K. Bhargava, Nanowire Morphology of Mono- and Bidoped α-MnO2Catalysts for Remarkable Enhancement in Soot Oxidation, ACS Appl. Mater. Interfaces. 9 (2017) 32652–32666. doi:10.1021/acsami.7b07656.

[42] T. Zhai, S. Xie, M. Yu, P. Fang, C. Liang, X. Lu, Y. Tong, Oxygen vacancies enhancing capacitive properties of MnO2nanorods for wearable asymmetric supercapacitors, Nano Energy. 8 (2014) 255–263. doi:10.1016/j.nanoen.2014.06.013.

[43] H. Chang, A.J. Bard, Scanning Tunneling Microscopy Studies of Carbon-Oxygen Reactions on Highly Oriented Pyrolytic Graphite, J. Am. Chem. Soc. 113 (1991) 5588–5596. doi:10.1021/ja00015a012.

[44] G.M. Bhalerao, A.K. Sinha, A.K. Srivastava, V. Sathe, G. Amarendra, Externally limited defect generation in multiwalled carbon nanotubes upon thermal annealing, and possible mechanism, Nanotechnology. 27 (2016). doi:10.1088/0957-4484/27/35/355706.

[45] N. Xu, Y. Liu, X. Zhang, X. Li, A. Li, J. Qiao, J. Zhang, Self-Assembly formation of Bi-functional Co 3 O 4 /MnO 2-CNTs hybrid catalysts for achieving both high energy/power density and cyclic ability of rechargeable zinc-Air battery, Sci. Rep. 6 (2016) 1–10. doi:10.1038/srep33590.

[46] A. Chatterjee, S. Or, Y. Cao, Transition Metal Hollow Nanocages as Promising Cathodes for the Long-Term Cyclability of Li–O2 Batteries, Nanomaterials. (2018). doi:10.3390/nano8050308.

[47] P. Tan, Z.H. Wei, W. Shyy, T.S. Zhao, X.B. Zhu, A nano-structured RuO_2 /NiO cathode enables the operation of non-aqueous lithium–air batteries in ambient air, Energy Environ.

Sci. 9 (2016) 1783–1793. doi:10.1039/C6EE00550K.

[48] Z. Sadighi, J. Liu, F. Ciucci, J.K. Kim, Mesoporous MnCo2S4 nanosheet arrays as an efficient catalyst for Li-O2 batteries, Nanoscale. 10 (2018) 15588–15599. doi:10.1039/c8nr03942a.

[49] Y. Shao-Horn, Y.C. Lu, Z.C. Xu, H.A. Gasteiger, S. Chen, K. Hamad-Schifferli, Platinum-Gold Nanoparticles: A Highly Active Bifunctional Electrocatalyst for Rechargeable Lithium-Air Batteries, J. Am. Chem. Soc. 132 (2010) 12170–12171. doi:10.1021/ja1036572.

[50] C. Tang, Y. Mao, J. Xie, Z. Chen, J. Tu, G. Cao, X. Zhao, $NiCo_2O_4$ /MnO_2 core/shell arrays as a binder-free catalytic cathode for high-performance lithium–oxygen cells, Inorg. Chem. Front. 5 (2018) 1707–1713. doi:10.1039/C8QI00062J.

[51] Y. Liu, F. Zhan, B. Wang, B. Xie, Q. Sun, H. Jiang, J. Li, X. Sun, Three-dimensional Composite Catalysts for Al-O2 Batteries Composed of CoMn2O4 Nanoneedles Supported on Nitrogen-Doped Carbon Nanotubes/Graphene, ACS Appl. Mater. Interfaces. 11 (2019) 21526–21535. doi:10.1021/acsami.9b04861.

[52] H. Cheng, K. Scott, Carbon-supported manganese oxide nanocatalysts for rechargeable lithium-air batteries, J. Power Sources. 195 (2010) 1370–1374. doi:10.1016/j.jpowsour.2009.09.030.

[53] B.D. McCloskey, A. Speidel, R. Scheffler, D.C. Miller, V. Viswanathan, J.S. Hummelshøj, J.K. Nørskov, A.C. Luntz, Twin problems of interfacial carbonate formation in nonaqueous Li-O 2 batteries, J. Phys. Chem. Lett. 3 (2012) 997–1001. doi:10.1021/jz300243r.

[54] R. Gao, L. Liu, Z. Hu, P. Zhang, X. Cao, B. Wang, X. Liu, The role of oxygen vacancies in improving the performance of CoO as a bifunctional cathode catalyst for rechargeable Li-O2batteries, J. Mater. Chem. A. 3 (2015) 17598–17605. doi:10.1039/c5ta03885e.

[55] K. Jin, A. Chu, J. Park, D. Jeong, S.E. Jerng, U. Sim, H.Y. Jeong, C.W. Lee, Y.S. Park, K.D. Yang, G.K. Pradhan, D. Kim, N.E. Sung, S.H. Kim, K.T. Nam, Partially oxidized sub-10 nm MnO nanocrystals with high activity for water oxidation catalysis, Sci. Rep. 5 (2015) 1–11. doi:10.1038/srep10279.

[56] P.W. Menezes, A. Indra, N.R. Sahraie, A. Bergmann, P. Strasser, M. Driess, Cobalt-manganese-based spinels as multifunctional materials that unify catalytic water oxidation and oxygen reduction reactions, ChemSusChem. 8 (2015) 164–167. doi:10.1002/cssc.201402699.

[57] R. Gao, L. Liu, Z. Hu, P. Zhang, X. Cao, B. Wang, X. Liu, The role of oxygen vacancies in improving the performance of CoO as a bifunctional cathode catalyst for rechargeable Li-O 2 batteries, J. Mater. Chem. A. 3 (2015) 17598–17605. doi:10.1039/c5ta03885e.

[58] A. Asokan, H. Lee, O. Gwon, J. Kim, O. Kwon, G. Kim, Insights Into the Effect of Nickel Doping on ZIF-Derived Oxygen Reduction Catalysts for Zinc−Air Batteries, ChemElectroChem. 6 (2019) 1213–1224. doi:10.1002/celc.201801827.

[59] Y. Xiong, Y. Yang, F.J. Disalvo, H.D. Abruña, Metal-Organic-Framework-Derived Co-Fe Bimetallic Oxygen Reduction Electrocatalysts for Alkaline Fuel Cells, J. Am. Chem. Soc. 141 (2019) 10744–10750. doi:10.1021/jacs.9b03561.

[60] S. Ratso, N. Ranjbar Sahraie, M.T. Sougrati, M. Käärik, M. Kook, R. Saar, P. Paiste, Q. Jia, J. Leis, S. Mukerjee, F. Jaouen, K. Tammeveski, Synthesis of highly-active Fe-N-C

catalysts for PEMFC with carbide-derived carbons, J. Mater. Chem. A. 6 (2018) 14663–14674. doi:10.1039/c8ta02325e.

[61] F. Tu, J. Xie, S. Zhang, G. Cao, T. Zhu, X. Zhao, Mushroom-like Au/NiCo2O4 nanohybrids as high-performance binder-free catalytic cathodes for lithium-oxygen batteries, J. Mater. Chem. A. 3 (2015) 5714–5721. doi:10.1039/c4ta06850e.

[62] K.R. Yoon, K. Shin, J. Park, S.H. Cho, C. Kim, J.W. Jung, J.Y. Cheong, H.R. Byon, H.M. Lee, I.D. Kim, Brush-Like Cobalt Nitride Anchored Carbon Nanofiber Membrane: Current Collector-Catalyst Integrated Cathode for Long Cycle Li-O2Batteries, ACS Nano. 12 (2018) 128–139. doi:10.1021/acsnano.7b03794.

[63] K.B. Knudsen, T. Vegge, B.D. McCloskey, J. Hjelm, An Electrochemical Impedance Spectroscopy Study on the Effects of the Surface- and Solution-Based Mechanisms in Li-O_2 Cells, J. Electrochem. Soc. 163 (2016) A2065–A2071. doi:10.1149/2.1111609jes.

[64] K.B. Knudsen, J.E. Nichols, T. Vegge, A.C. Luntz, B.D. McCloskey, J. Hjelm, An Electrochemical Impedance Study of the Capacity Limitations in Na-O2Cells, J. Phys. Chem. C. 120 (2016) 10799–10805. doi:10.1021/acs.jpcc.6b02788.

[65] F.S. Gittleson, K.P.C. Yao, D.G. Kwabi, S.Y. Sayed, W.H. Ryu, Y. Shao-Horn, A.D. Taylor, Raman Spectroscopy in Lithium-Oxygen Battery Systems, ChemElectroChem. 2 (2015) 1446–1457. doi:10.1002/celc.201500218.

[66] I. Landa-Medrano, I. Ruiz De Larramendi, N. Ortiz-Vitoriano, R. Pinedo, J. Ignacio Ruiz De Larramendi, T. Rojo, In situ monitoring of discharge/charge processes in Li-O2 batteries by electrochemical impedance spectroscopy, J. Power Sources. 249 (2014) 110–117. doi:10.1016/j.jpowsour.2013.10.077.

[67] L. Johnson, C. Li, Z. Liu, Y. Chen, S.A. Freunberger, P.C. Ashok, B.B. Praveen, K. Dholakia, J.M. Tarascon, P.G. Bruce, The role of LiO 2 solubility in O 2 reduction in aprotic solvents and its consequences for Li-O 2 batteries, Nat. Chem. 6 (2014) 1091–1099. doi:10.1038/nchem.2101.

[68] J. Huang, B. Zhang, Z. Bai, R. Guo, Z.L. Xu, Z. Sadighi, L. Qin, T.Y. Zhang, G. Chen, B. Huang, J.K. Kim, Anomalous Enhancement of Li-O2Battery Performance with Li2O2Films Assisted by NiFeOxNanofiber Catalysts: Insights into Morphology Control, Adv. Funct. Mater. 26 (2016) 8290–8299. doi:10.1002/adfm.201603178.

[69] D. Aurbach, B.D. McCloskey, L.F. Nazar, P.G. Bruce, Advances in understanding mechanisms underpinning lithium-air batteries, Nat. Energy. 1 (2016) 1–11. doi:10.1038/nenergy.2016.128.

[70] Y. Xu, X. Wang, C. An, Y. Wang, L. Jiao, H. Yuan, Facile synthesis route of porous $MnCo_2O_4$ and $CoMn_2O_4$ nanowires and their excellent electrochemical properties in supercapacitors, J. Mater. Chem. A. 2 (2014) 16480–16488. doi:10.1039/C4TA03123G.

[71] Z. Lyu, Y. Zhou, W. Dai, X. Cui, M. Lai, L. Wang, F. Huo, W. Huang, Z. Hu, W. Chen, Recent advances in understanding of the mechanism and control of Li 2 O 2 formation in aprotic Li-O 2 batteries, Chem. Soc. Rev. 46 (2017) 6046–6072. doi:10.1039/c7cs00255f.

[72] K.N. Jung, S.M. Hwang, M.S. Park, K.J. Kim, J.G. Kim, S.X. Dou, J.H. Kim, J.W. Lee, One-dimensional manganese-cobalt oxide nanofibres as bi-functional cathode catalysts for rechargeable metal-air batteries, Sci. Rep. 5 (2015) 1–10. doi:10.1038/srep07665.

[73] B.G. Kim, H.J. Kim, S. Back, K.W. Nam, Y. Jung, Y.K. Han, J.W. Choi, Improved reversibility in lithium-oxygen battery: Understanding elementary reactions and surface

charge engineering of metal alloy catalyst, Sci. Rep. 4 (2015). doi:10.1038/srep04225.

[74] L. Lai, J.R. Potts, D. Zhan, L. Wang, C.K. Poh, C. Tang, H. Gong, Z. Shen, J. Lin, R.S. Ruoff, Exploration of the active center structure of nitrogen-doped graphene-based catalysts for oxygen reduction reaction, Energy Environ. Sci. 5 (2012) 7936–7942. doi:10.1039/c2ee21802j.